# Rotating Stall Suppression Using Oscillatory Blowing Actuation on Blades

Final Report
GRANT #FA9550-07-1-0187
Principal Investigators: Paul G. A. Cizmas and Othon K. Rediniotis
Graduate Students: Forrest Carpenter and Shalom Johnson

Date Report was Issued: June 30, 2010

Texas Engineering Experiment Station
Office of Sponsored Research
332 Wisenbaker Engineering Research Center, 3000 TAMU
College Station, Texas 77843-3000

| | | |
|---|---|---|
| **Report Documentation Page** | | *Form Approved*<br>*OMB No. 0704-0188* |

Public reporting burden for the collection of information is estimated to average 1 hour per response, including the time for reviewing instructions, searching existing data sources, gathering and maintaining the data needed, and completing and reviewing the collection of information. Send comments regarding this burden estimate or any other aspect of this collection of information, including suggestions for reducing this burden, to Washington Headquarters Services, Directorate for Information Operations and Reports, 1215 Jefferson Davis Highway, Suite 1204, Arlington VA 22202-4302. Respondents should be aware that notwithstanding any other provision of law, no person shall be subject to a penalty for failing to comply with a collection of information if it does not display a currently valid OMB control number.

| 1. REPORT DATE<br>**30 JUN 2010** | 2. REPORT TYPE | 3. DATES COVERED |
|---|---|---|

| 4. TITLE AND SUBTITLE<br>**Rotating Stall Suppression Using Oscillatory Blowing Actuation on Blades** | 5a. CONTRACT NUMBER<br>**FA9550-07-1-0187** |
|---|---|
| | 5b. GRANT NUMBER |
| | 5c. PROGRAM ELEMENT NUMBER |
| 6. AUTHOR(S)<br>**Paul Cizmas; Othon Rediniotis** | 5d. PROJECT NUMBER |
| | 5e. TASK NUMBER |
| | 5f. WORK UNIT NUMBER |
| 7. PERFORMING ORGANIZATION NAME(S) AND ADDRESS(ES)<br>**Texas Engineering Experiment Station,Office of Sponsored Research,332 Wisenbaker Engineering Research Center, 3000 TAMU,College Station,TX,77843-3000** | 8. PERFORMING ORGANIZATION REPORT NUMBER |
| 9. SPONSORING/MONITORING AGENCY NAME(S) AND ADDRESS(ES) | 10. SPONSOR/MONITOR'S ACRONYM(S) |
| | 11. SPONSOR/MONITOR'S REPORT NUMBER(S) |

12. DISTRIBUTION/AVAILABILITY STATEMENT
**Approved for public release; distribution unlimited.**

13. SUPPLEMENTARY NOTES

14. ABSTRACT

**Highly maneuverable aircraft require that the propulsion system (jet engine) operates during sudden accelerations and rapid changes in inlet conditions. Consequently, the compressor of the jet engine occasionally must operate at low flow rates and high angles of attack. The high-angle- of-attack low-flow regime of compressor operation is often plagued by rotating stall and surge. Rotating stall and surge cannot be tolerated during compression operation because: (1) they can be catastrophic to engine performance, (2) they cause rapid heating of the blades, and (3) they can induce severe mechanical stresses. Traditional methods for surge and separation control have included: (1) use of bleed-air off-take, (2) use of variable inlet guide vanes and variable inlet stator vanes, and (3) casing air injection upstream of the blade tip.**

15. SUBJECT TERMS

| 16. SECURITY CLASSIFICATION OF: | | | 17. LIMITATION OF ABSTRACT | 18. NUMBER OF PAGES | 19a. NAME OF RESPONSIBLE PERSON |
|---|---|---|---|---|---|
| a. REPORT<br>**unclassified** | b. ABSTRACT<br>**unclassified** | c. THIS PAGE<br>**unclassified** | | **38** | |

**Standard Form 298 (Rev. 8-98)**
Prescribed by ANSI Std Z39-18

# Contents

# List of Figures

# List of Tables

# Abstract

Highly maneuverable aircraft require that the propulsion system (jet engine) operates during sudden accelerations and rapid changes in inlet conditions. Consequently, the compressor of the jet engine occasionally must operate at low flow rates and high angles of attack. The high-angle-of-attack low-flow regime of compressor operation is often plagued by rotating stall and surge. Rotating stall and surge cannot be tolerated during compression operation because: (1) they can be catastrophic to engine performance, (2) they cause rapid heating of the blades, and (3) they can induce severe mechanical stresses. Traditional methods for surge and separation control have included: (1) use of bleed-air off-take, (2) use of variable inlet guide vanes and variable inlet stator vanes, and (3) casing air injection upstream of the blade tip.

We proposed to interrupt the propagation of stall cells by using oscillatory blowing actuation on rotor blades. The experimental investigation of oscillatory blowing actuation on cascade blades, supported by numerical simulation, demonstrated the capability of stall supression in a linear cascade. A crucial element of this flow control system was the pulse generator. This pulse generator uses the compressor rotation movement to generate high frequency oscillatory blowing actuation on the suction side of the airfoil. A scaled-down version of the pulse modulator was built and tested to ensure that the design would achieve the required flow parameters.

Several experiments were conducted with the scaled-down pulse modulator. Two sets of experiments studied the frequency response and the flow characteristics of the jet slot. Subsequently, a small wind tunnel with a linear cascade has been built around the scaled-down pulse modulator. These experiments studied the effects that oscillatory blowing had on the pressure distribution on the upper surface of a NACA 0015 airfoil section.

The frequency response experiment proved that, within the operating range of this compressor test rig and for reduced frequencies close to unity, jet frequency did not have a significant effect on the jet momentum coefficient, $C_\mu$. The experimental investigation showed that jet slot exit area must match the area of the inlet to the internal plenum of the blade to obtain the $C_\mu$ values that are required to effectively suppress stall. It was also shown that the distribution of the holes in the internal pipe played an important role in the spanwise $C_\mu$ distribution, but it did not affect the mean $C_\mu$ value.

A subsequent experiment investigated the effect of oscillatory blowing actuation on a NACA 0015 in a wind tunnel that was build for a linear cascade of airfoils. In this experiment the pressure distribution on the suction side of the airfoil was measured with and without flow actuation. The investigation without oscillatory blowing actuation showed that (1) inner walls are needed to eliminate the non-uniform flow in the cascade and (2) the airfoil stalled between 12 and 13 degrees. When oscillatory blowing actuation was used, the lift coefficient increased by 51% to 98% and the angle-of-attack at stall increased by at least 5 deg.

Therefore, the experimental investigation conducted on the scaled-down pulse modulator demonstrated that it is worth building and testing the full-size pulse modulator for the compressor. Additional work is needed to understand the flow physics of the high frequency interaction between the oscillatory blowing actuation and the stall cell in order to suppress rotating stall.

# Chapter 1

# Introduction

Stall and surge are problems that plagued compressors for as long as turbomachinery have been built. Although considerable progress has been made in understanding and modeling these phenomena, they continue to be a major challenge for turbomachinery designers. This report describes the research activities focused toward developing a new approach to eliminate or delay rotating stall and surge by using oscillatory blowing actuation on the compressor (rotor) blades. A brief description of rotating stall and surge is given in the following paragraphs.

As the compressor mass flow rate is reduced, the pressure rise increases up to a point beyond which a further reduction of the mass flow rate results in a sudden change in the flow pattern. If the mass flow is reduced beyond this catastrophic point, the compressor enters into either stall or surge. Regardless of whether the compressor goes into stall or surge, the point of instability is called the *surge point*. Depending on the geometry and load of the compressor, the stall could be progressive (a small drop in performance) or abrupt (a very large drop in the pressure ratio and mass flow). In both cases, the flow is no longer axisymmetric but has a circumferentially non-uniform pattern of regions of separated flow, which rotate around the annulus.

The regions of separated flow are called stall cells. There may be one or more stall cells, and the cells may extend from hub to casing (full-span stall) or only over part of the span (part-span stall). The blockage generated by a stall cell leads to a reduction of angle of attack on one side of the cell and an increase on the other side. As a result, the stall cell, which could cover more than one blade passage, moves along the circumference with a fraction of the wheel speed. This phenomenon, in which the total flow rate through the annulus does not vary with time, is called rotating (or propagating) stall. Rotating stall was first reported for centrifugal compressors and then for axial compressors.

Surge, on the other hand, is defined as the phenomenon where the net flow through the entire annulus fluctuates with time. Violent flow instabilities during surge include symptoms such as audible thumping and honking at inlet and exit, at frequencies as low as 1 Hz, and severe mechanical vibrations. Certainly, violent surge cannot be tolerated in an aircraft jet engine because of the danger of mechanical failure or interruption of the combustion process.

Research into understanding compression system instabilities began with the low-order, hydrodynamic stability model of rotating stall and surge developed by Moore and Greitzer (1986). This model was developed for an incompressible, undistorted flow field. The model consists of a set of three simultaneous nonlinear third-order partial differential equations for pressure rise, average and disturbed values of flow coefficient, as functions of time and circumferential angle. This model provided the theoretical framework for understanding how to suppress rotating stall and surge using active control (Epstein et al., 1989). More recently, a reduced-order model of the unsteady viscous

flow in a compressor cascade has been developed, which is ideally suited for the design of active control strategies to suppress rotating stall (Florea et al., 1997, 1998).

Rotating stall has been shown to be a two-dimensional or three-dimensional form of instability (Day, 1993b). Surge, on the other hand, has traditionally been regarded as a one-dimensional disturbance with axisymmetric velocity fluctuations affecting all parts of the system (Greitzer, 1978). Rotating stall is limited to blade rows and depends only on the compressor, while surge involves the entire pumping system: compressor, throttles, ducting and plenums (Paduano et al., 1993). Recent experimental results have revealed that rotating stall plays an important part in initiating a surge event, particularly for highly loaded axial compressors (Day, 1993b). Consequently, delaying rotating stall also delays surge.

Day (1993a) used a system of twelve casing-mounted air valves to generate damping disturbances by injecting small puffs of air into the main stream near the tips of the first rotor in a four-stage axial compressors. The valves were opened and closed 120 times per second, that is, 12 times faster than the rotational frequency of the modal perturbations. The improvement in the stalling flow coefficient was 4%. A 23% reduction of the stalling mass flow of a low-speed, single-stage, axial research compressor was obtained by "wiggling" the inlet guide vanes to generate circumferentially traveling waves with appropriate phase and amplitude to control the first three spatial harmonics (Silkowski, 1990; Paduano et al., 1993).

The casing-mounted air valves provided a simpler actuation mechanism compared to the moving inlet guide vanes. It is somewhat difficult to judge how much more effective were the moving inlet guide vanes compared to the casing-mounted air valves because they were applied to different compressors, a single-stage and a four-stage, respectively. Certainly the effectiveness of the casing injection was reduced because it affected mainly the flow at the tip of the blades.

Steady mass injection upstream of the tip of a high-speed compressor rotor reduced the stalling flow coefficient at design speed by 6% using an injected mass flow equivalent to 2% of the annulus flow (Suder et al., 2001). Larger reductions of the stalling flow coefficient were obtained at reduced percent speeds. For compressors operating at part speed for extended periods of time, however, tip injection is not a viable option because the aerodynamic performance is reduced due to the efficiency penalty incurred using tip injection (Suder et al., 2001).

Unsteady injection on the suction side of a compressor stator airfoil in a linear cascade was used to reduce the total pressure loss by 65%, when the injected mass flow rate was 1.6% of the freestream mass flow rate (Carter et al., 2001). Steady and unsteady injection was also used on the suction side of a stator airfoil in a four-stage low-speed compressor. In this case, a 25% reduction in area-averaged loss was obtained when the injected mass flow rate was 1% of the compressor through-flow (Culley et al., 2004).

## 1.1   Limits of current practice in stall and surge suppression

The methods currently used to suppress surge and stall are: (1) bleed off-take, (2) active control of variable inlet guide vane and variable stator vanes, and (3) casing air injection upstream of the blade tip.

The inter-stage bleeds remove a portion of the air at an intermediate stage and dump the bleed air into the bypass flow. As a result, energy is wasted through the work done to compress the (bleed) air that is then not used for combustion.

The variable inlet guide vanes and variable stator vanes are quite complex, require power to operate and add to the overall weight of the engine. In addition, the variable vanes are not fail-save and their malfunction can severely affect engine performance.

Air tip injection could be implemented in a jet engine, but the efficiency penalty incurred using tip injection makes it inapplicable to compressors that operate at part speed for extended duration. Furthermore, the mass flow rate of air that needs to be injected in order to prevent flow separation in the hub region is significantly larger than the amount of air needed locally to prevent separation.

# Chapter 2

# Research Activities

We propose to interrupt the propagation of the stall cell(s) by using oscillatory blowing actuation on one rotor blade per row. There is ample experimental and numerical evidence that jet actuation on isolated airfoils increases the stall angle. Therefore, herein it was hypothesized that when a stall cell reaches a blade with jet actuation, the stall cell will either (a) diminish and reduce its circumferential velocity or (b) entirely vanish, depending on the relative values of the stall angle of the blade with jet actuation and the angle of attack that drives the stall cell. This section summarizes the activities that were completed during this project: (1) the design and testing of a compressor blade row, (2) the design of the internal plenum for the flow control blade, (3) the design and fabrication of the pulse modulator, (4) the design and fabrication of a low-speed linear cascade for testing blade flow actuation, and (5) the fabrication of the linear cascade blades and the testing of jet actuation effect on blades.

## 2.1   Compressor Blade Design

A set of rotor and stator blades were designed for the compressor test rig at Texas A&M University. This was done to facilitate the manufacture of the flow control blade, known herein as the "super-blade". The blades were designed for a 1.5-stage axial flow, low speed compressor shown in Fig. 2.1. The compressor is powered by either a 20 or 100 HP electric motor which spins at an operating velocity of 3,500 RPM. The compressor has a blade count of 16:25:32. The blades were designed with a flow coefficient of 0.4, a hub-to-tip ratio of 0.6, a constant chord of 0.0762 m (3 in), and an aspect ratio of 1.33.

A free-vortex radial distribution was initially chosen for the compressor blades. The free-vortex method produced a rotor blade with a large variation in stagger angle in the spanwise direction. It was decided that the large amount of twist would increase the difficulty of the manufacturing of the internal plenum of the super-blade. As a result, a set of compressor blades using the original design parameters and a forced-vortex radial distribution were designed (Johnson et al., 2008). Using the forced-vortex radial distribution greatly reduced spanwise variation of the stagger angle as illustrated in Fig. 2.2. The red blade in Fig. 2.2 was designed using the free-vortex method, and the transparent blue blade with the forced-vortex method.

The airfoil thickness distributions of both the rotor and the stator vary from a NACA 65-0012 at the hub to a NACA 65-0008 at the tip. The airfoil thickness distributions were fitted to parabolic camber lines defined by the blade inlet and exit flow angles. The thickness distributions were chosen so that a plenum and orifices could be easily machined for the super-blade. The rotor blade airfoils were stacked with respect to a point on the camber line at a distance of 0.40 chords from the leading

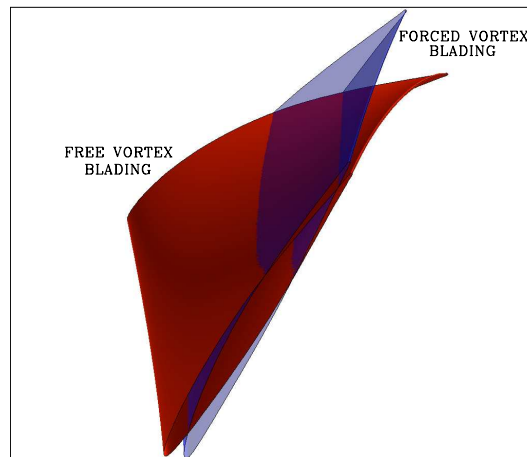Figure 2.1: TAMU 1.5 stage low speed axial flow compressor.



Figure 2.2: Blade design comparison).

edge of the blade cross-section. The stator blade airfoils were stacked at a distance of 0.50 chords from the leading edge.

### 2.1.1 Compressor Blade Flow Simulation

Computational fluid dynamics (CFD) was used to verify the new rotor and stator designs. The NASA grid generator TCGRID was used to discretize the compressor. TCGRID is a three-dimensional grid generation code that creates C-type grids around the blade, and has the option for H-type grid inlets and O-type grids for tip clearance regions (Chima, 2003b). An inlet H-type grid and O-type grids for tip clearance regions are used for all of our CFD simulations.

The flow through the discretized domain was solved using SWIFT. SWIFT is a multi-block code for the analysis of three-dimensional viscous flows in turbomachinery (Chima, 2003a). The code solves the thin layer Navier-Stokes equations using an explicit finite-difference technique. A variable time-step and implicit residual smoothing were used for convergence acceleration. The Baldwin-Lomax turbulence model was used for all of the simulations conducted with SWIFT.

Initial simulations were completed on a single row system (rotor only) before moving on to simulating the actual multi-row system. A sample grid of the single row system that was initially simulated can be seen in Fig. 2.3 through Fig. 2.5. Multi-row simulations were completed to capture the interaction between the rotor and the stator. An example of the meshes used can be seen in Fig. 2.6.

#### 2.1.1.1 Grid Convergence Study

A grid convergence study for the multi-row system was completed to ensure the independence of the solution from the mesh. Four meshes of varying refinement were generated for this study. An equal number of blades in each row was assumed to reduce the computational effort. This provided a blade count for the computational domain of 32:32. As a result, the rotor was scaled by a factor of 25/32. The sizes for the different meshes generated are presented in Table 2.1.

A Courant-Friedrichs-Lewy (CFL) number of 0.5 was used in the calculation of the solutions for all four of the meshes presented in Table 2.1. The simulations were run until the mass flow rate error was found to be less than one percent. The number of iterations required for all four cases
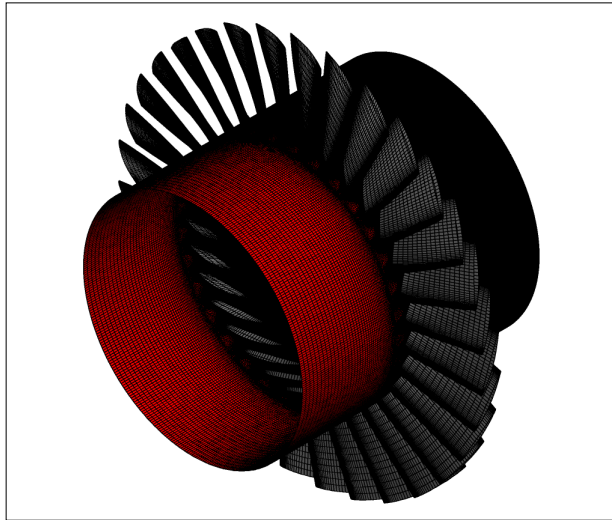
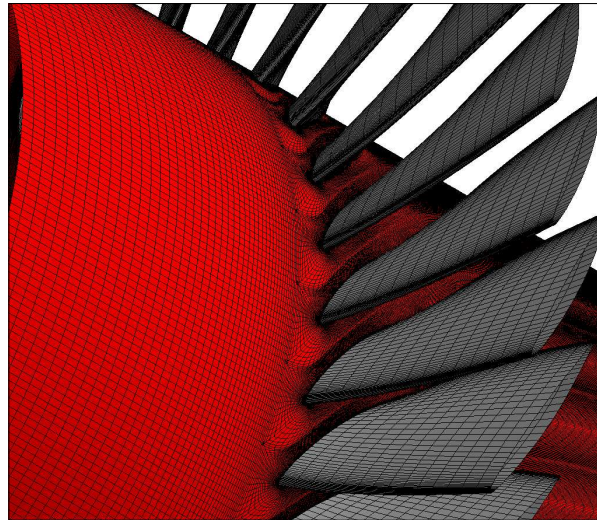Figure 2.3: Full view of single row system.



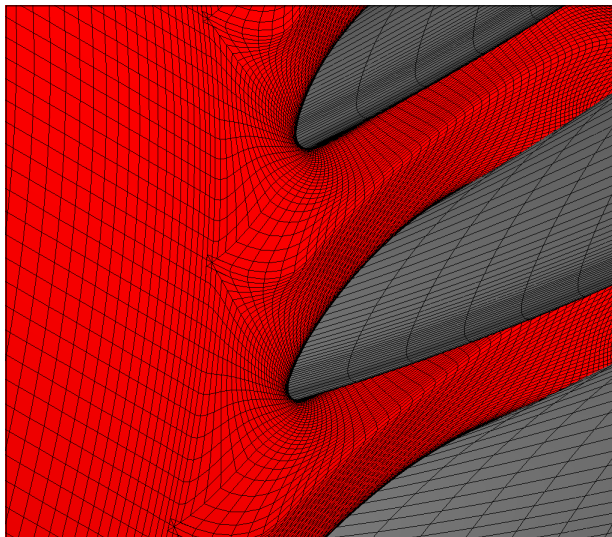Figure 2.4: Rotor blade zoom (single row system).



Figure 2.5: Rotor blade leading edge zoom (single row system).
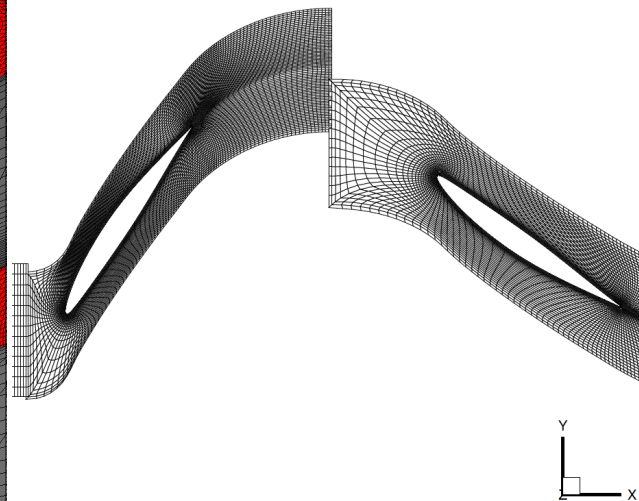


Figure 2.6: Mid-span layer of compressor mesh.

to achieve this convergence criterion was on the order of 70,000 iterations. The solution residuals were also monitored to gauge the convergence of the solution. The lift generated at the mid-span of the rotor was calculated to judge the independence of the solution from the mesh size. The trend shown in Fig. 2.7 indicated that the solution was independent of the mesh size due to the convergent trend of the curve. As a result, Mesh 3 was used for all remaining simulations.

### 2.1.2 Compressor Stage Design

A parametric study was completed in SWIFT to find the best blade design for the given compressor geometry. Three parameters were varied in this study: (1) the total-to-total pressure ratio, $\pi^*$, (2), the flow coefficient, $\phi$, and (3) the degree of reaction, $\rho_c$. A stage design was chosen based on the results from the different test cases of the parametric study. The chosen parameters of the

Table 2.1: Grid convergence mesh dimensions.

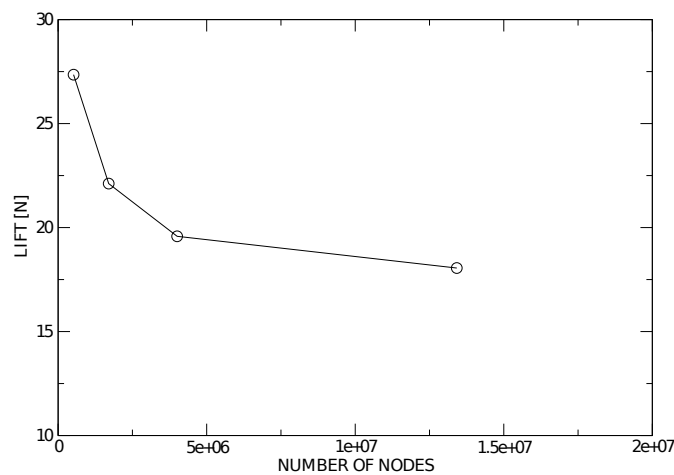|  | Mesh 1 | Mesh 2 | Mesh 3 | Mesh 4 |
|---|---|---|---|---|
| Inlet H-Grid | 45x12x45 | 67x18x67 | 90x24x90 | 135x36x135 |
| Rotor C-Grid | 122x34x45 | 183x54x67 | 244x68x90 | 366x102x135 |
| Rotor O-Grid | 87x13x13 | 130x13x13 | 173x13x13 | 259x13x13 |
| Stator C-Grid | 170x37x45 | 255x56x67 | 340x74x90 | 510x111x135 |
| Stator O-Grid | 71x13x13 | 106x13x13 | 141x13x13 | 211x13x13 |
| **Total** | **520,712** | **1,702,757** | **4,005,146** | **13,417,700** |



Figure 2.7: Mid-span lift variation with mesh size.

compressor stage are shown in Table 2.2.

Table 2.2: Stage Parameters

| | |
|---|---|
| Outer Diameter, $D_o$[mm] | 505.7 |
| Hub-to-Tip Ratio, $\zeta$ | 0.6 |
| Inlet Flow Angle, $\alpha_{1,m}$ | $20°$ |
| Flow Coefficient, $\phi$ | 0.4 |
| Pressure Ratio, $\pi^*$ | 1.02 |
| Degree of Reaction, $\rho_c$ | 0.754 |

### 2.1.3 Blade Fabrication

The manufacturing technology required for blade fabrication was determined during the blade design. Two different construction techniques were decided upon. The first called for the construction of composite blades for experimental validation of the blade design. The composite blade consists of a metal skeleton with rapid prototype material used to provide the complex blade shape. A composite blade prototype can be seen in Fig. 2.8. This method of construction does not allow for

the fabrication of a "super-blade" due to the inability to cut flow control jets into the blade.

The second fabrication technique uses the investment casting method to construct metal blades. The investment casting method allows the blades to be constructed out of aluminum while maintaining a ±0.254 mm (±0.01 in) tolerance. The aluminum construction also allows the cutting of the internal plenum and flow control jets of the "super-blade" through the use of 5-axis electrical discharge machining (EDM). A model of an aluminum "super-blade" can be seen in Fig. 2.9.

In both fabrication methods, a conventional dovetail design was utilized for the blade and disk interface (See Fig. 2.8 and Fig. 2.9). The conventional dovetail design allows the disk to be manufactured using a CNC mill.

Figure 2.8: Composite blade prototype.

Figure 2.9: "Super-blade" model.

### 2.1.4  Structural Analysis

Preliminary stress calculations were performed to aid the material selection process for the stage two rotor blades and the disk. Aluminum A357.0 T6 was chosen for the stage two rotor blades and AISI 301$\frac{1}{2}$ Hard Stainless Steel for the disk. Material properties for these materials can be found in Military Handbook 5H and are not repeated here. Preliminary centrifugal force calculations were performed on the stage two rotor blades, the dovetail attachment, and on the disk. The dovetail attachment and disk were designed in an iterative process using the results from the preliminary stress analysis. The preliminary stress analysis results were satisfactory: the stress due to centrifugal forces on the blade alone was 59 daN/cm$^2$, the stress due to the normal force on the dovetail attachment was 60 daN/cm$^2$, and the stress due to the centrifugal force on the disk was 83 daN/cm$^2$.

Using the results from the preliminary stress analysis, a finite element analysis (FEA) model was constructed using ABAQUS (ABAQUS Inc., 2006). Rotational forces were accounted for by the FEA model. The analysis was divided into two parts: (1) the disk attachment and (2) the aluminum blade and dovetail attachment. The disk attachment model was discretized using an unstructured grid containing 101,000 elements. The disk attachment model accounts for the normal stress due to the dovetail attachment and centrifugal forces. The FEA stress results for the disk attachment can be seen in Fig. 2.10. The safety factor calculated based on the FEA analysis was found to be greater than 10 for the disk.

The aluminum blade and dovetail attachment model was discretized using an unstructured grid containing 108,000 elements. The blade and dovetail attachment model was constrained at the

dovetail attachment and loaded with centrifugal forces. The FEA stress results can for the blade and dovetail model can be seen in Fig. 2.11. The results yielded a safety factor greater than five for the blade and dovetail assembly.
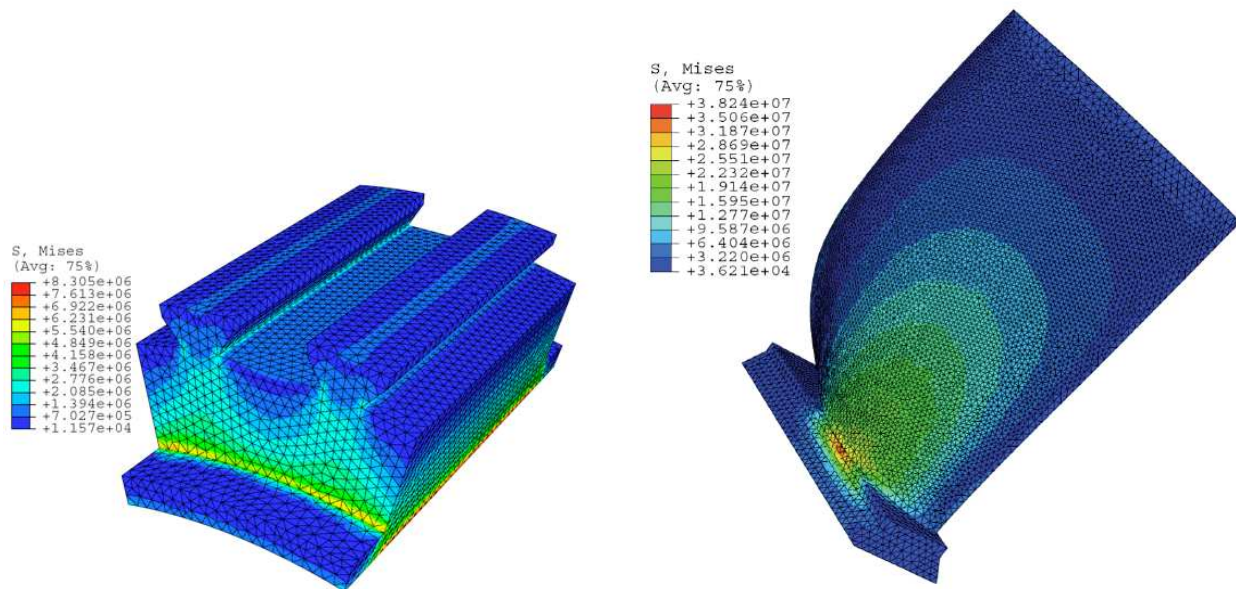


Figure 2.10: Disk attachment FEA stress results in Pascals.

Figure 2.11: Aluminum blade and dovetail FEA stress results in Pascals.

Due to the complexity of the non-isotropic characteristics of the rapid prototype material, the composite blade design was not model using FEA. Instead of a numerical analysis, the structure of the composite blade prototype was tested experimentally. The blade was spun in a CNC mill to determine what effect the centrifugal and aerodynamic forces had on the structure. A photo of the test setup can be seen in Fig. 2.12. The prototype blade was successfully spun up to a RPM that exceed the maximum operating speed of the compressor test rig by 22% with no visible structural damage.

## 2.2   Internal Plenum Design

The internal plenum of the "super-blade" bridges the gap between the pulse modulator buried within the compressor and the flow control actuation jets on the surface of the blade. The size and shape of the plenum greatly influences the complexity of the system and its frequency response. This section presents the design evolution of the internal plenum.

### 2.2.1   First Generation Design

A numerical study was completed on the preliminary geometry of the internal plenum. This analysis was done using FLUENT, a commercial flow simulation package. The preliminary geometry for the internal plenum of the super-blade encompassed the entire usable volume of a generic rotor blade and incorporated a single injection slot that ran the span of the blade. Two assumptions were made to simplify the calculations: the internal flow was assumed to be steady and laminar. These assumptions were removed during later CFD simulations used to refine the design of the internal

Figure 2.12: Composite blade structural test setup.

plenum.

The CFD velocity results for the preliminary model are shown in Fig. 2.13 and Fig. 2.14. Figure 2.13 shows that a single-vane was required to achieve a uniform span-wise velocity distribution. Figure 2.14 shows that there is no variation of the chord-wise component of the velocity in the span-wise direction. The uniform chord-wise component is beneficial when the stall cell spans the entire blade.

## 2.2.2  Second Generation Design

It was decided that an internal plenum with a smaller volume and individual injection jet orifices would eliminate the need for internal vanes (which were needed by the first generation design) and improve the frequency response of the system. The new internal plenum is modeled by a small diameter pipe which spans the length of the blade and a contracting inlet, as shown in Fig. 2.15. The inlet contracts the flow cross-sectional area from the cross-sectional area of the pulse modulator slots to the cross-sectional of the plenum within the "super-blade". The contraction inlet region of the internal plenum is contained with in the disk of the compressor.

Numerical simulations were used to refine the internal plenum geometry. An in-house, three-dimensional Reynolds-averaged Navier-Stokes (RANS) solver was used to calculate the flow within the internal plenum. The code was initially developed for turbomachinery flows (Han and Cizmas, 2003), and has been used for aeroelastic applications (Gargoloff et al., 2006). Turbulence was modeled using the Shear Stress Transport (SST) model (Menter, 1994). A hybrid structured and unstructured grid was used to discretize the domain (Carpenter et al., 2009). Mach contours for a preliminary single hole plenum can be seen in Fig. 2.16. The velocity profiles exhibited by the exit jet flow were found to be similar to those predicted by Schlichting's plane laminar jet approximations (White, 2006).
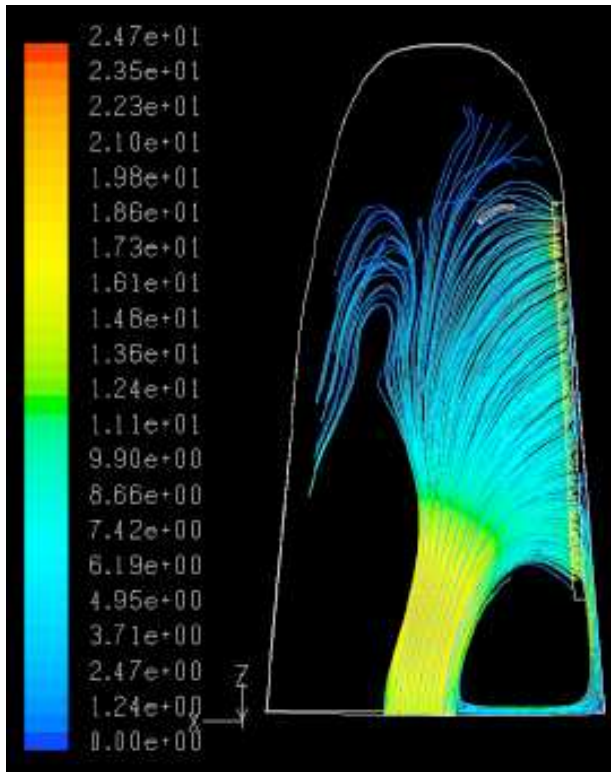
Figure 2.13: Blade internal flow.
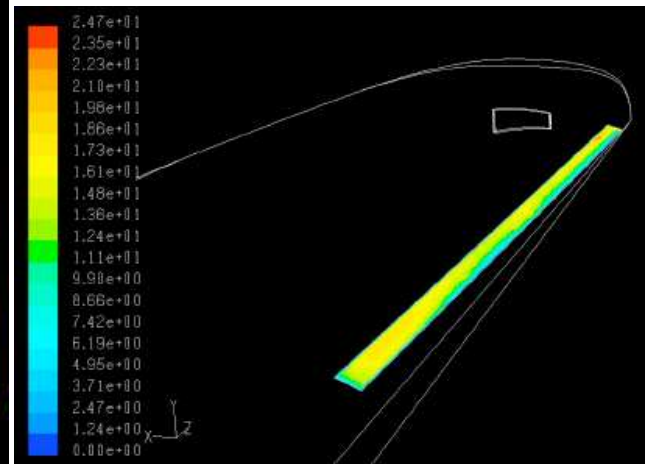


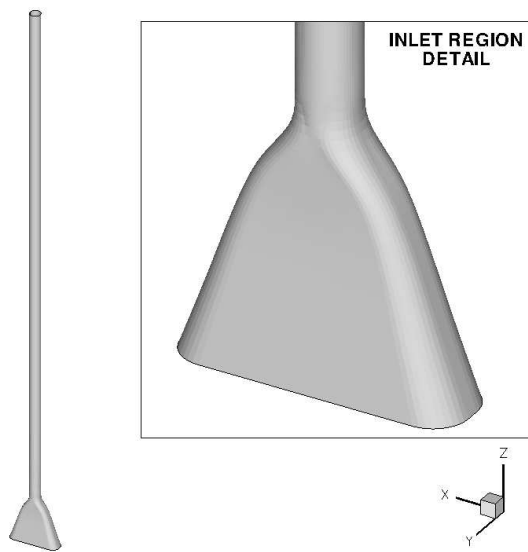Figure 2.14: Injection slot velocity contours.



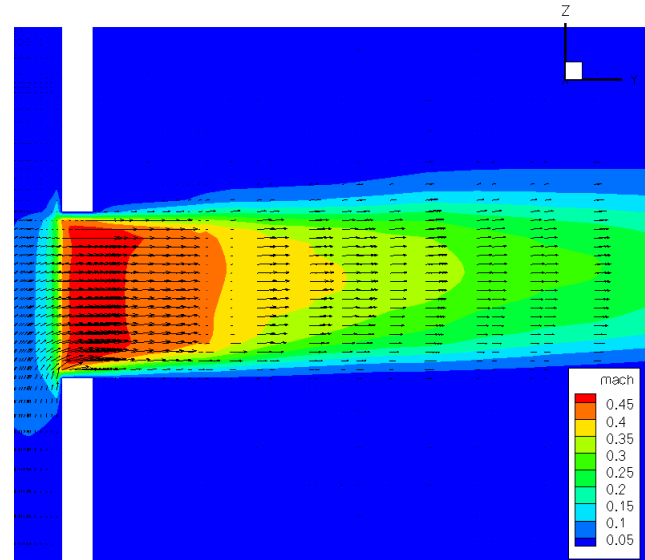Figure 2.15: Second generation internal plenum design.



Figure 2.16: Single exit jet Mach contours.

## 2.3  Pulse Modulator Design

The pulse modulator is the flow control system component that supplies the "super-blade" with oscillatory blowing air. The geometry of the pulse modulator impacts the frequency of flow control

actuation as well as the mass flow rate. This section presents the design evolution of the pulse modulator and the construction of a miniature pulse modulator for proof of concept experiments.

### 2.3.1   First Generation Design

The first generation pulse modulator design consisted of two components: (1) a fixed component attached to the frame and (2) a rotating component attached to the disk. The fixed component is further broken down into two sub-components, a fixed base and a fixed plate. The fixed base is bolted to the structure of the compressor on the intake side. Holes in the fixed plate and the rotating plate allow for an impulse of air to pass through. When mounted, the two components create an air cavity between them that is fed by an air line passing through the fixed base. The fixed component can be seen in the right side of the photograph of the prototype pulse modulator in Fig. 2.17.

Similarly to the fixed component, the rotating component of the pulse modulator can be broken down into a rotating plate and a rotating base. The rotating base is mounted to the disk with the rotating plate mounted to the rotating base. When fully assembled, the rotating plate and the fixed plate almost make contact. A thrust bearing is located between the two plates to allow low-friction rotation of the device. The rotating plate has a hole that aligns periodically with the holes in the fixed plate. The periodic alignment of the holes generates the oscillatory blowing air. The air pulse is passed onto the "super-blade" via a connecting tube. The rotating component of the pulse modulator is shown on the left side of Fig. 2.17.



Figure 2.17: First generation pulse modulator prototype.

### 2.3.2  Second Generation Design

The first generation pulse modulator design did not provide a desirable reduced excitation frequency. As a result, the pulse modulator was redesigned to meet the reduced excitation frequency requirements while satisfying the other design constraints, e.g., geometric limitations and manufacturability.

The reduced excitation frequency is described by the dimensionless frequency $F^+ = f_{jet}x_{te}/U_\infty$ where $f_{jet}$ is the actuation frequency, $x_{te}$ is the distance from the trailing edge of the blade to the actuation jet, and $U_\infty$ is the freestream velocity. Acceptable $F^+$ values vary over a range of 0.5 to 5.0. The lower end of the range was selected to be the design requirement for the flow control system. As a result, the pulse modulator was designed to provide a $F^+$ of 0.5 at the tip of the "super-blade", with larger values being generated towards the hub.

The second generation pulse modulator was designed to be an integral part of the compressor disk. Using the disk removes the requirement of the additional rotating component of the pulse modulator. The design of the pulse modulator is shown in Figs. 2.18 and 2.19. The design consists of the disk and the pulse modulator. The internal wall of the compressor disk is tapered to allow the pulse modulator, which is also tapered, to fit inside. A spacer (see Fig. 2.18) is used to adjust the clearance between the disk and pulse modulator. The tight fit provides a virtual seal between the disk and pulse modulator. The pulse modulator is mounted on a ball bearing that is attached to the disk. The bearing allows the the disk to rotate while the pulse modulator remains stationary.
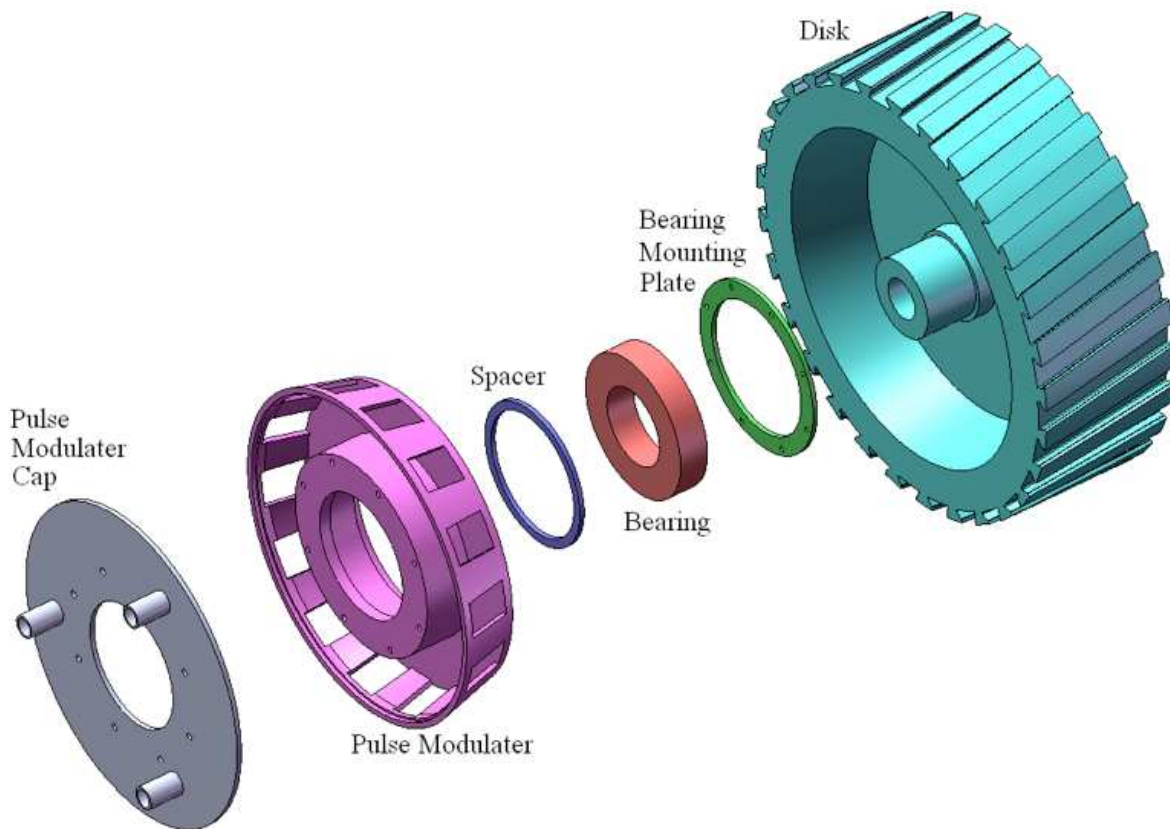


Figure 2.18: Second generation pulse modulator exploded view.

Compressed air is supplied to the system via air hoses connected to the stationary pulse modulator. The rotating disk has one slot that periodically lines up with the holes cut into the pulse modulator as shown in Fig. 2.19. The periodic alignment provides the "super-blade" with the required $f_{jet}$ value. The value of $f_{jet}$ can be modified by changing the hole distribution.

The mass flow rate through the virtual seal created by the gap between the pulse modulator and disk was investigated before the design of the pulse modulator was finalized. This was done due to the effect that the leakage has on the minimum velocity of actuation during one cycle. An experiment was conducted using a testbed that models one segment of the pulse modulator. A schematic of the test bed is shown in Fig. 2.20. The test used hot wire measurements to determine the velocity of air leaking between the disk and pulse modulator for several clearances and inlet pressures. The test was also used to determine the optimal clearance to be used in the pulse modulator. The clearance was chosen to be 0.8 mm (0.003 in).
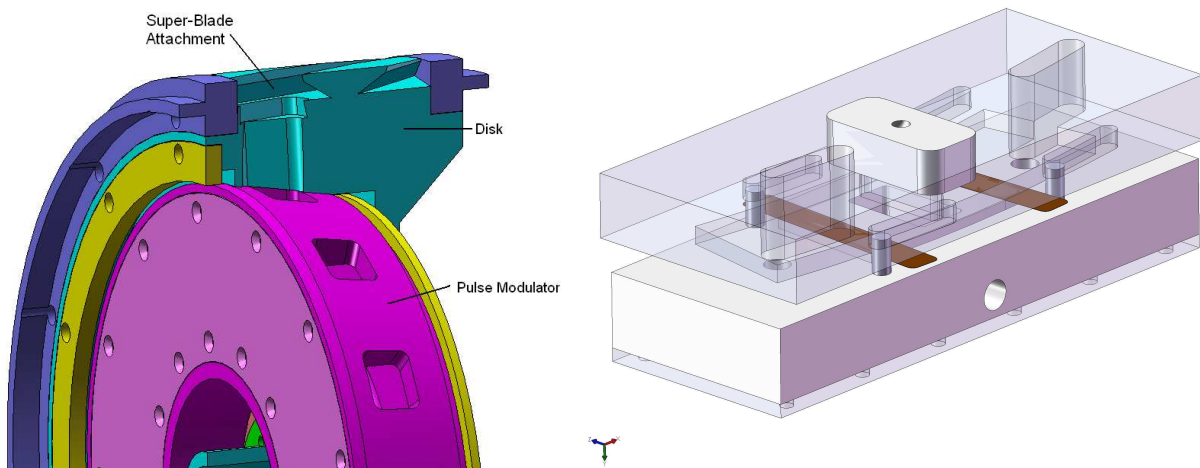


Figure 2.19: Second generation pulse modulator cur-away.

Figure 2.20: Drawing of the pulse modulator test bed.

### 2.3.3   Scaled-Down Pulse Modulator

A scaled-down version of the second generation pulse modulator was designed and built to provide proof of concept for the design and to serve as a testbed for internal plenum designs (Carpenter et al., 2009). The miniature pulse modulator was also used to supply oscillatory blowing air to the linear cascade wind tunnel which is described in section 2.4. A photograph of the miniature pulse modulator test bed is shown in Fig. 2.21.

The miniature pulse modulator produces the pulse width modulated air supply in a similar fashion to the full scale version. The primary differences between the two being that the casing of the miniature pulse modulator, which is analogous to the compressor disk in the full scale version, remains stationary while the pulse modulator is spun instead. The size of the internal plenum which is contained by the compressor disk in the full scale version is maintained by the miniature version. The inlet region of the internal plenum is constructed using a rapid prototype insert that can be easily removed and replaced. The inlet insert is connected to the miniature pulse modulator via a slot cut into the casing and an aluminum plate.

Construction of the miniature pulse modulator testbed provided important understanding of the manufacturing techniques required to construct the full scale version. The testbed also showed

that the tight clearances required of the full scale version could be maintained during operation. Additionally, the miniature pulse modulator proved that the required $F^+$ numbers could be achieved by this design.
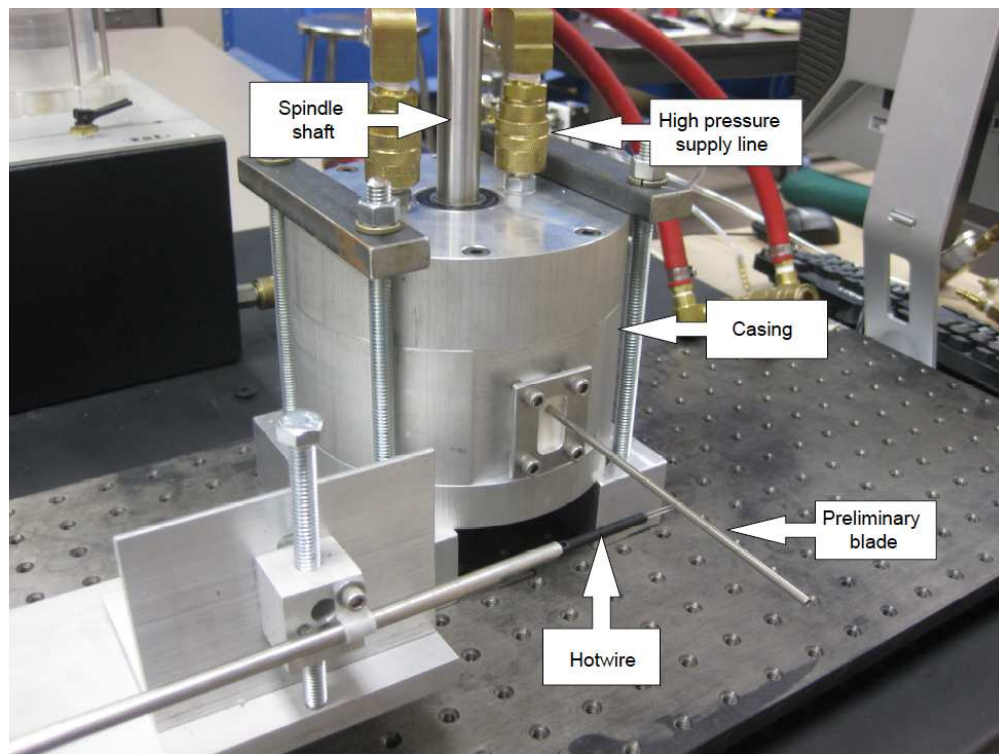


Figure 2.21: Scaled-down pulse modulator testbed.

## 2.4    Wind Tunnel for Linear Cascade

A wind tunnel for a linear cascade was designed and built to study the effect of the pulsing air on the suction side of airfoils in cascades. This step was necessary in order to understand the effect of flow control on blades in a linear cascade prior to applying the flow control in the rotating cascade of the compressor. This wind tunnel and linear cascade were designed to fit inside a CNC mill, in order to use the CNC mill spindle to provide the actuation for the pulse modulator. The airfoils of the linear cascade were designed such that the internal plenum of the test blade matched the full-size pulse modulator that will be used in the axial compressor.

The wind tunnel for the linear cascade is shown in Fig. 2.22. The main components of the wind tunnel are the inlet and flow conditioner, the cylinder that holds the blades (called blade cylinder), the pulse modulator, the angle-of-attack mechanism, the diffuser, and the fan. The pulse modulator was spun by either a drill press (for small reduced excitation frequencies $F^+$) or by the CNC mill spindle (for larger $F^+$ numbers).

The shape of the inlet is described by the fifth-order polynomial $y = 6.10 \cdot 10^{-3}x^5 - 3.66 \cdot 10^{-4}x^4 + 6.05 \cdot 10^{-6}x^3 - 7.03 \cdot 10^{-3}x^2 - 0.148x + 3.91$ where the units of $x$ and $y$ are inches, and $x$ varies between 4 and 20 inches. The inlet is 609.6-mm (24-in) long and 155.58-mm (6.125-in) wide and has a flat 101.6-mm (4-in) section before and after the polynomial contraction. There is a 19-mm-thick honeycomb flow conditioner on the front of the inlet.
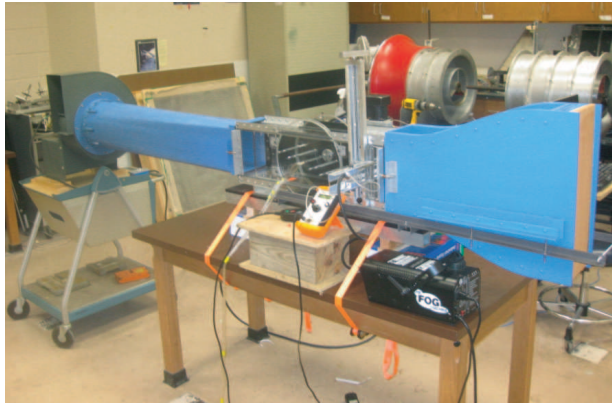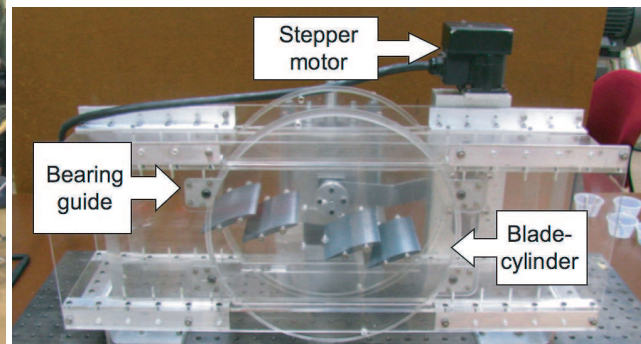
Figure 2.22: Wind tunnel for linear cascade.



Figure 2.23: Blade cylinder.

The linear cascade has an inner and outer set of walls. The advantages of using two sets of walls are: (1) the boundary layer, which is formed in the inlet, is absorbed in the gap between the inner and outer walls, and therefore it does not interfere with the flow over the airfoil, and (2) the leakage around the blade cylinder is reduced by the small pressure difference between the test section and the gap between the walls.

The blade cylinder, shown in Fig. 2.23, is the cylinder on which the airfoils are installed. The stagger angle of the cascade is modified by rotating the cylinder. The cylinder has an aluminum bracket on the pulse modulator side of the cascade, which is supported by a ball bearing on the outer wall. The bracket is also connected to the angle-of-attack (or better said, stagger angle) arm, as shown in Fig. 2.24. The angle-of-attack arm is used to rotate the blade cylinder. The front side of the cylinder is supported with four ball bearing around the perimeter of the cylinder, as shown in Fig. 2.25. This support configuration allows unobstructed visual access to the airfoil surface, which is needed for flow visualization.
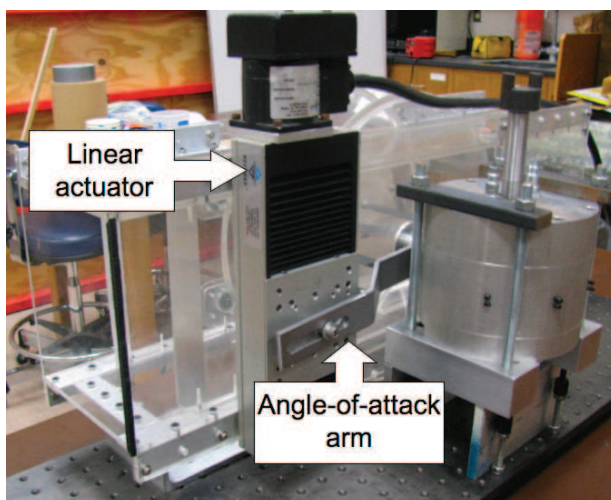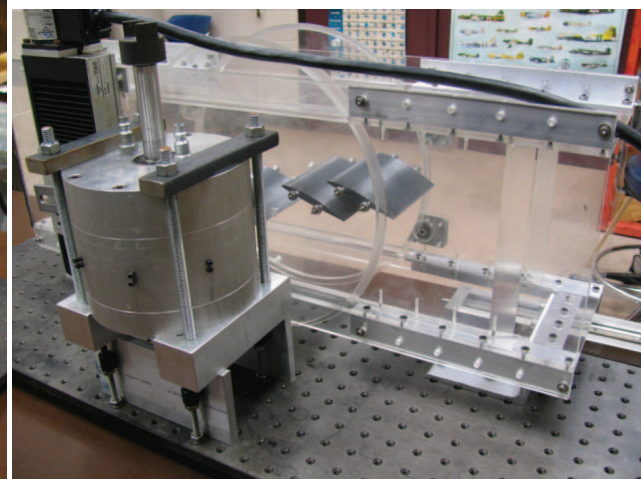


Figure 2.24: Angle-of-attach controller.



Figure 2.25: Scaled-down pulse modulator attached to linear cascade.

A Barocell pressure transducer was used to measure the pressure in the linear cascade. A scanivalve was used to switch to all the pressure ports. There were eleven pressure ports on the

top surface of the airfoil, and a total pressure measurement from a Pitot tube located upstream of the blades. All of the pressures were relative to the static pressure of the Pitot tube. The Pitot tube was mounted to the top of the tunnel, and the height of the Pitot tube was adjustable. This mounting system could also be installed to the side of the linear cascade.

The angle-of-attack (or stagger angle) of the cascade is adjustable and is controlled with a stepper motor. The stepper motor drives a ball-screw assembly that rotates the blade cylinder, as shown in Fig. 2.24. The angle-of-attack was calibrated using a digital protractor. The protractor was aligned with the chord line using an alignment tool, which has a bottom surface that is exactly the same shape as the upper surface of the airfoil and a top surface that is aligned with the chord line. The alignment tool was made using a rapid-prototype machine.

The diffuser is a fiber glass cylinder that smoothly transitions from the rectangular test-section, 177.6 by 155.6 mm, to the round fan inlet, 244.5 mm diameter. This diffuser has an area ratio of 1.70, and an equivalent diffuser angle of 1.42 deg. The length of the diffuser was determined by the size of the CNC mill.

The fan uses a centrifugal compressor and has a 1.12 kW (1.5 hp) electric motor. The fan has a volumetric flow rate of approximately 1,290 l/s (2,230 cfm) and generates in the wind tunnel a velocity between 32 to 38 m/s (72 to 85 mph). The mass flow rate of the fan was not adjustable. Therefore, the velocity was varied by varying the blockage of the wind tunnel.

## 2.5   Flow Control Experiment

This section presents details about the test blades and traversing system used in this experiment, the investigation of the jet frequency response, jet characteristics and the overall effect of oscillatory blowing actuation on airfoils in cascade.

### 2.5.1   Test Blades

The test blade designed and built for the linear cascade had the same dimensions as the compressor blade: 76.2 mm (3 in) chord and 101.6 mm (4 in) span. The airfoil used for the test blade was a NACA 0015. The blade tested in the linear cascade had no turning. This test blade had an internal plenum that was identical to that of the super-blade that will be used in the axial compressor.

The test blade had eleven pressure ports along the chord, which were located on a diagonal across the top surface of the blade, as shown in Fig. 2.26. These pressure ports were used to measure the pressure distribution on the suction side of the test blade. The plumbing consisted of stainless steel hypodermic tubes and Teflon plastic tubes, as shown in Fig. 2.27. The plastic tubes were plumbed to the upper surface of the blade. The plastic tubes were then trimmed flush with the top surface of the test-blade. The plumbing chamber was then filled with epoxy and sanded to match the bottom surface of the test-blade.

Two internal pipes were made for the test-blade: one had holes along the entire span, and one had holes only along the central part of the blade span. The pipe with holes along the entire span had 93 0.66-mm diameter holes distributed evenly across the full span of the blade, as shown in Fig. 2.28. The holes were spaced 1.04 mm apart. The other pipe had 20 0.66-mm diameter holes that were located along the central part of the blade span. These holes were also spaced 1.04 mm apart.

The test blade has a slot that runs along the span, as shown in Fig. 2.29, and it is connected to the pipe that supplies the pulsing air. The slot was sanded to be 0.127-mm wide. The area of the jet slot along the entire blade span, projected onto the velocity coming out of the pipe, is 12.9 mm$^2$. Figure 2.30 shows the wing fences mounted on the test blade in the wind tunnel. These

(a) Jet slot and pressure ports locations

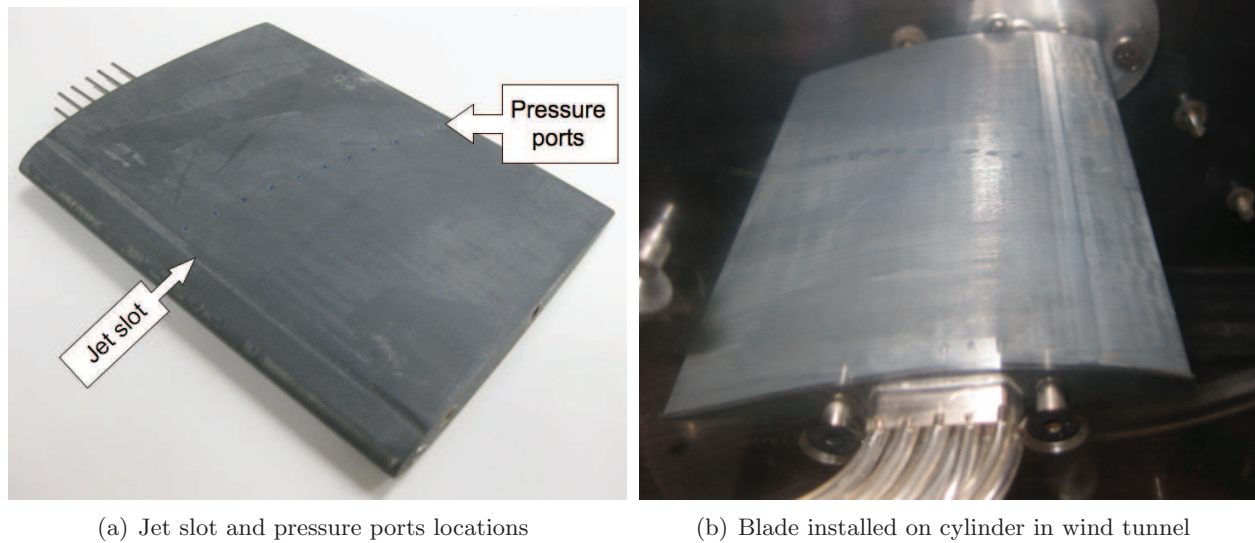(b) Blade installed on cylinder in wind tunnel
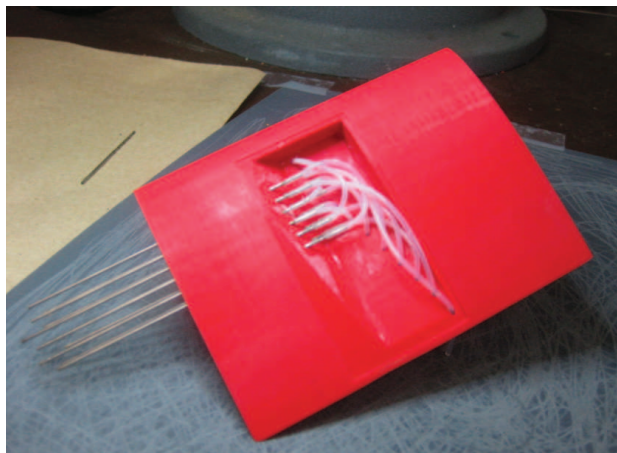
Figure 2.26: Test blade.



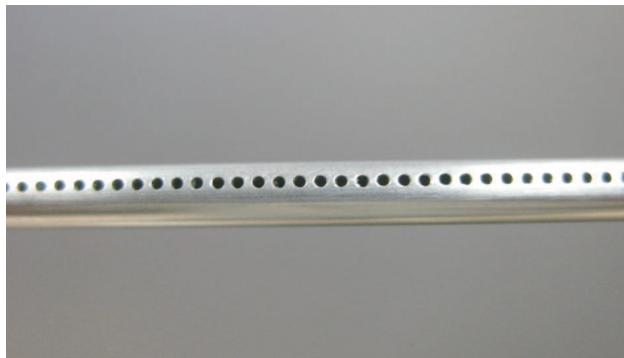Figure 2.27: Test blade pressure ports plumbing.

Figure 2.28: Detail of the pipe.

fences were used to test the airfoil with flow control operating only along the central part of the blade span.

The velocity in the vicinity of the slot was measured using a hot-wire probe with a three-axis traversing system. A second experiment was conducted where the velocity at the exit of a slotted pipe, shown in Fig. 2.31, was measured with a hot-wire probe mounted on a single-axis traversing system.

### 2.5.2   Traversing System Description

The single-axis traversing system consisted of a stepper motor that drove a linear actuator. The system was controlled using an Aerotech UNIDEX 12 system that was connected to the main computer via a serial port. The traversing system was commanded by a Labview code. This allowed the movement to be coordinated with the hot-wire measurement. The stepper motor was
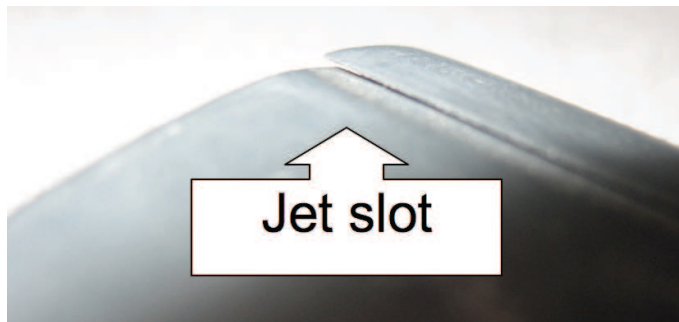
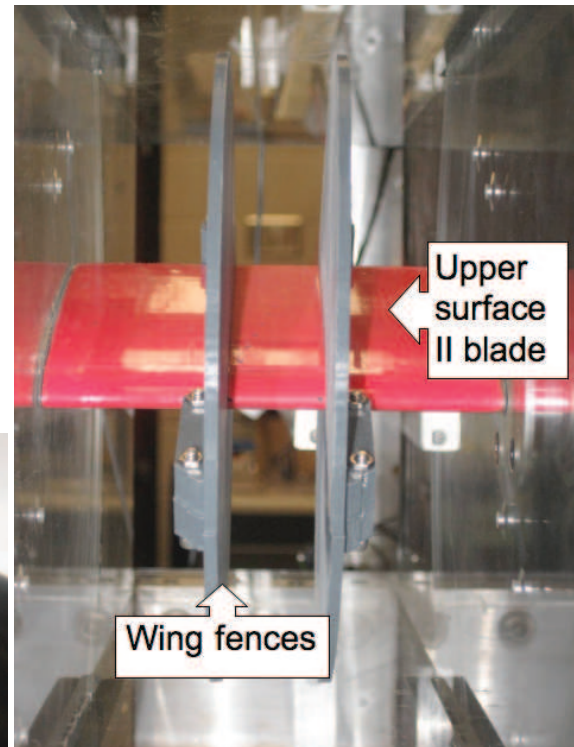Figure 2.29: Detailed view of the jet slot.



Figure 2.30: Wing fences mounted on test blade (with the neighboring airfoils removed).



(a) Attachment and pipe
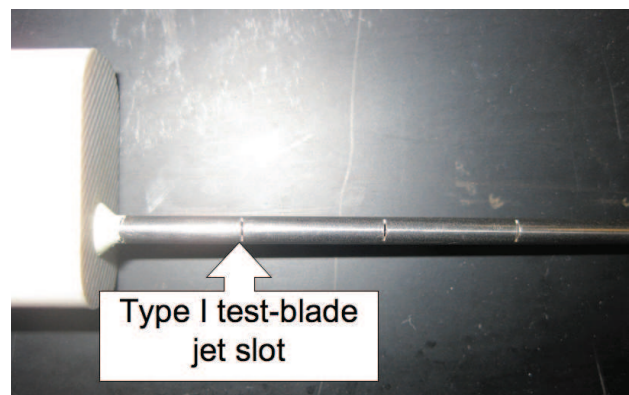


(b) Jet slot details

Figure 2.31: Pipe with slots.

equipped with an angular encoder, which ensured that there were negligible location errors. The linear actuator was equipped with a home switch, thus allowing the system to retain the relative location after a power-cycle. The one-axis traversing system is shown in Fig. 2.32.

The three-axis traversing system, shown in Fig. 2.33, was built in-house. All of the axes were controlled with a ball-screw assembly; however, only two of the axes were driven with a stepper motor. The third axis was hand operated. The two automated axes were equipped with limit switches that were also used to home each axis. An Aero-probe controller was used to operate the

Figure 2.32: Single-axis traversing system.



Figure 2.33: Three-axis traversing system.
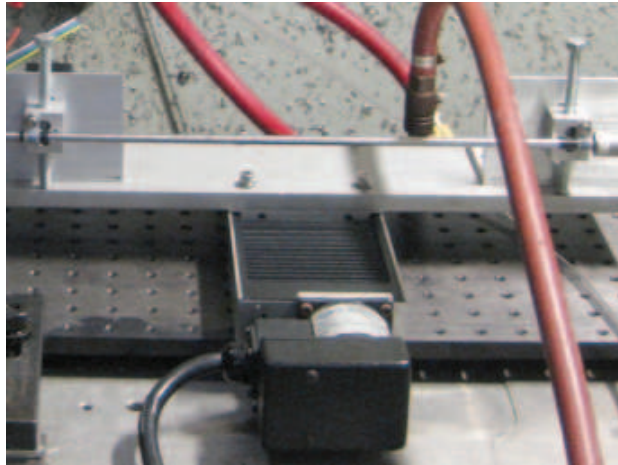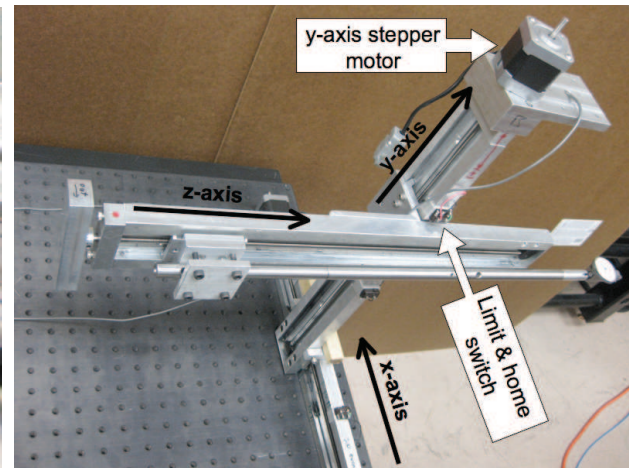
stepper motors. A driver for this controller was written in Labview. Thus the traversing system was controlled via a Labview code. This system had no position feedback; therefore, it needed to be homed periodically to prevent location errors from accumulating.

### 2.5.3 Jet Frequency Response Experiment

The slotted pipe shown in Fig. 2.31, was used to investigate the effect of the jet frequency on the amplitude of the pulses. This frequency response test was primarily done to investigate the change in jet momentum coefficient $C_\mu$ with frequency. In this test the jet velocity was measured while varying the $F^+$ number and the pressure at the pulse modulator. The experiment was conducted in a CNC mill, as shown in Fig. 2.34. The CNC mill spindle was used to spin the pulse modulator. This allowed us to test a wide range of angular velocities for the pulse modulator.

The pipe with slots had the same dimensions as the pipe used inside the test blade, that is, 3.35-mm outer diameter, 3-mm inner diameter, and 114-mm length. The hot-wire anemometer was
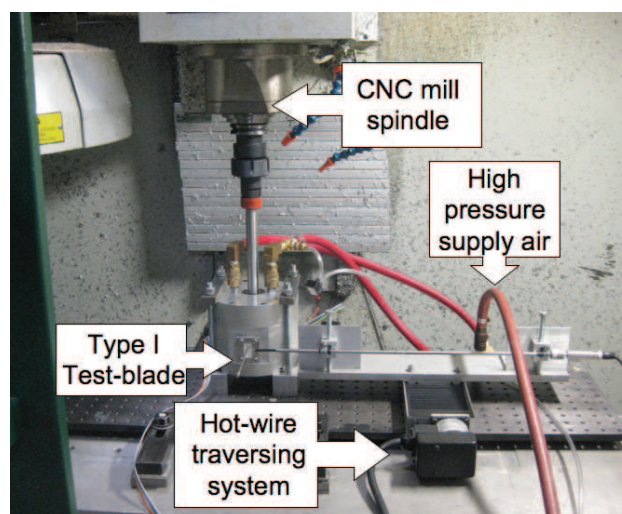


Figure 2.34: Experimental setup for exit frequency response.

used to measure the high frequency jet velocity. The hot-wire was aligned with the slots of the
pipe, such that the hot-wire was completely submerged in the flow exiting the jet slot.

Table 2.3: Pipe jet test matrix.

| Supply pressure, $p$ [psi] | 1.19, 2.57, 3.81 |
|---|---|
| Wheel speed, $n$ [rpm] | 500 to 6000 with increments of 500 |
| Jet frequency, $f_{jet}$ [Hz] | 66.6 to 800 with increments of 66.6 |
| Spanwise location across hole, $x$ [mm] | 25 location sweeping across each hole with an increment $\Delta x$ of 0.031 mm |

Several values of the angular velocity and supply pressure were used, as shown in Table 2.3. The
variation of jet momentum coefficient $C_\mu$ as a function of dimensionless frequency $F^+$, spanwise
location $R$ and supply pressure $p$ is shown in Fig. 2.35. These results indicate that the variation of
the jet momentum coefficient $C_\mu$ with the reduced excitation frequency $F^+$ is small. In addition,
$C_\mu$ decreases as the distance between inlet and hole increases. The variation of $C_\mu$ with pressure is
small, for the range of pressures tested herein. Furthermore, the variation of $C_\mu$ with $F^+$ decreases
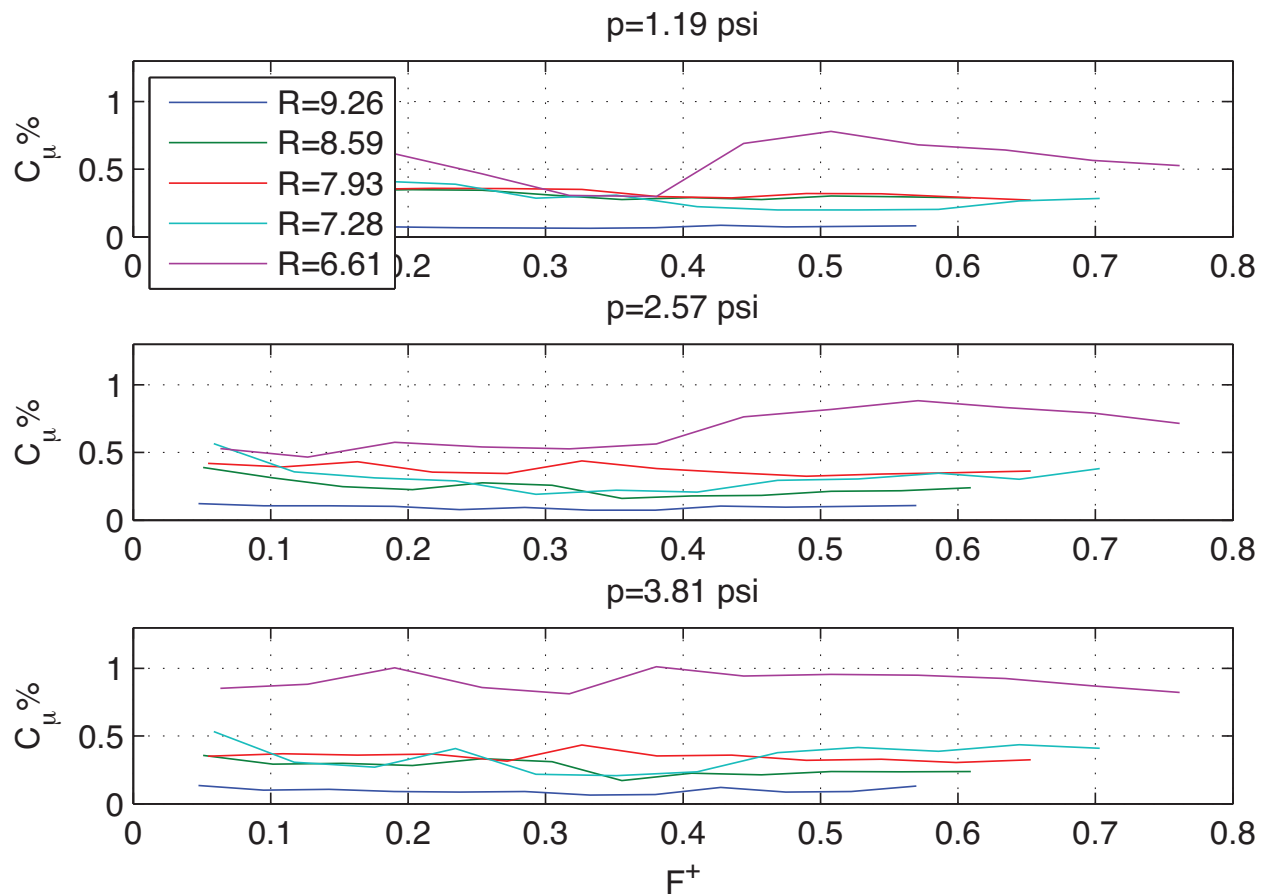when pressure increases.



Figure 2.35: Jet momentum coefficient $C_\mu$ vs. dimensionless frequency $F^+$. $R$ denotes the hole
spanwise location, in inches.

The $C_\mu$ versus hole span for different supply pressure and for an $F^+$ number of 0.47, at the tip of the blade, is shown in Fig. 2.36. The rest of the plots corresponding to all the $F^+$ numbers will be included in the final report. This plot shows higher amplitudes for the holes near the inlet.
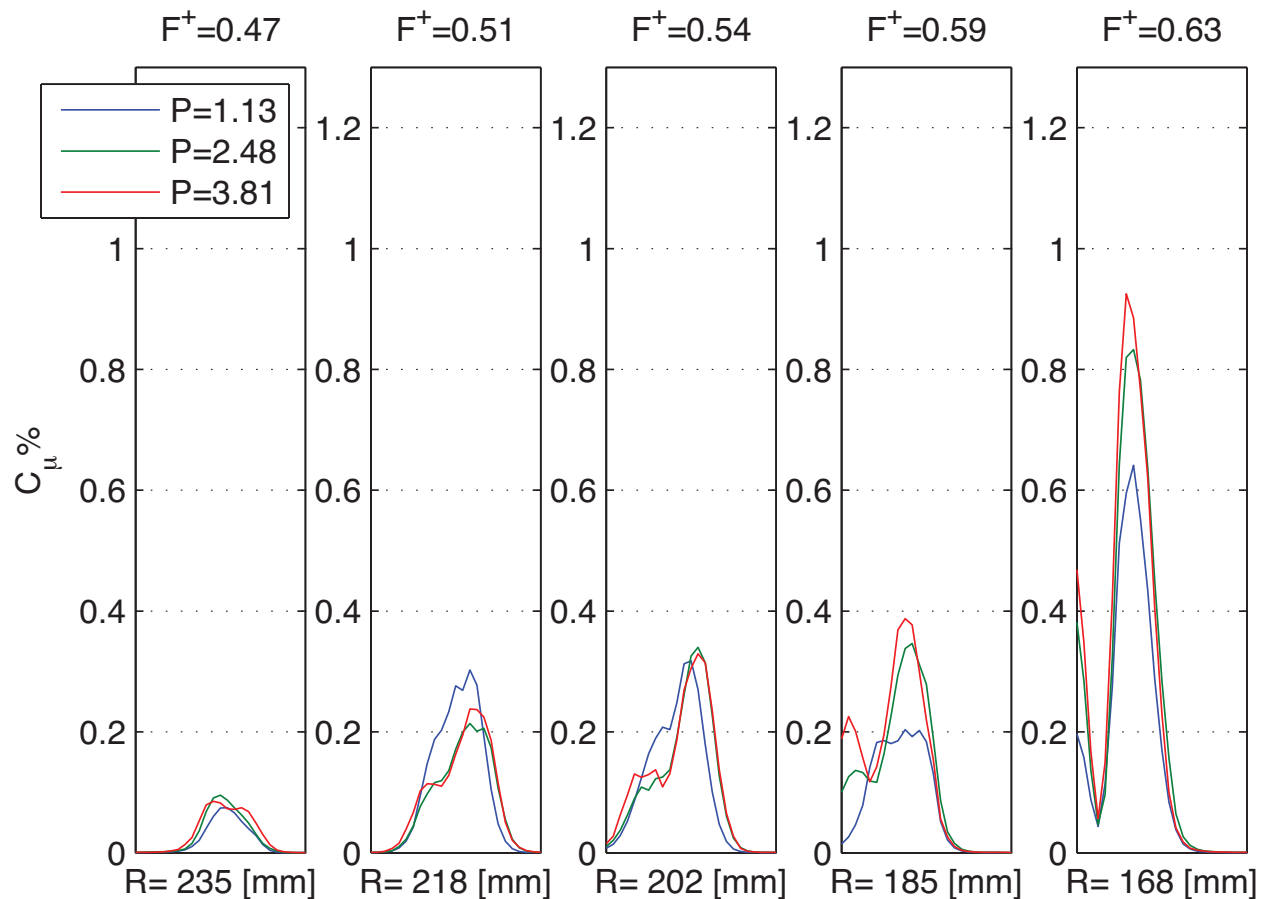


Figure 2.36: Jet momentum coefficient $C_\mu$ vs. dimensionless frequency $F^+$. $R$ denotes the hole spanwise location, in inches.

### 2.5.4   Jet Characteristics Experiment

This experiment was conducted to study the effect of the jet slot on the linear cascade test blade at different supply pressures and multiple internal pipe configurations. The experiment provided the range of $C_\mu$ values obtainable by the miniature pulse modulator and test blade setup. The experiment was conducted in the cascade wind tunnel with the exit diffuser and motor removed. This was done to prevent any changes in exit flow characteristics between this experiment and the actual flow control experiment.

A hot wire probe mounted to the three-axis traversing system was used to sweep over the jet slot in both the spanwise and chordwise directions. Aligning the traversing system with the test blade was accomplished by using a test indicator. The height of the hot wire probe above the surface of test blade was adjusted by hand, and as a result, the repeatability in height was $\pm0.125$ mm. A photograph of the hot wire probe in position for an experiment can be seen in Fig. 2.37.

Three different internal pipe configurations were examined, one full span pipe and two different
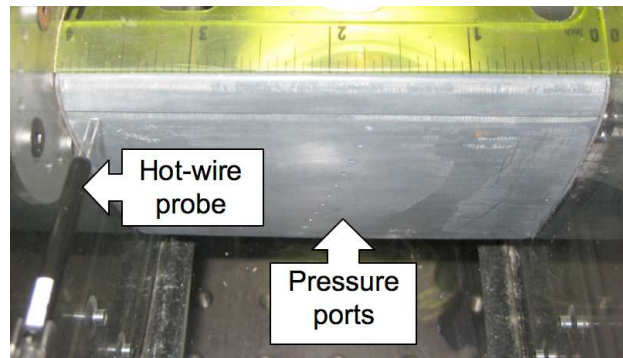
Figure 2.37: Aligned hot wire probe.

partial span pipes. Two different partial span pipes were tested because a drilling error led to the misalignment of the holes in the original partial span pipe. The flawed pipe was tested to see what effects the irregular hole pattern had on the $C_\mu$ distribution. The full span pipe will be referred to herein as FSP, and the flawed and correct partial span pipes are labeled herein as PSP1 and PSP2, respectively.

The hot wire probe was swept in increments of 1.01 mm along the spanwise direction, and in increments of 0.127 mm in the chordwise direction. The movement of the hot wire and data collection was handled by a LabView program. The spanwise axis of the traversing system was homed after every spanwise sweep to prevent location errors. The chordwise axis of the traversing system homed at the end of a full chordwise sweep. The test matrix listing all experiments is shown by Table 2.4.

Table 2.4: Jet slot test matrix.

| Pipe Configuration | Supply Pressure [psi] | | | | | Spanwise Location [mm] | | Chordwise Location [mm] | |
|---|---|---|---|---|---|---|---|---|---|
| | | | | | | Min | Max | Min | Max |
| Full | | | | | 25 | 5.05 | 85.3 | 0.00 | 0.76 |
| Partial (flawed) | 5 | 10 | 15 | 20 | 25 | 38.7 | 56.0 | 0.00 | 0.76 |
| Partial | 5 | 10 | 15 | 20 | 25 | 38.7 | 56.0 | 0.00 | 0.76 |

The standard deviation of the jet velocity was calculated for all spanwise and chordwise locations. The maximum chordwise value of the standard deviation was used to calculate the spanwise distribution of $C_\mu$. The $C_\mu$ calculations were done for every case given in Table 2.4. The freestream and jet conditions needed for $C_\mu$ calculations were taken from cascade wind tunnel, and are summarized in Table 2.5. The spanwise $C_\mu$ distributions for each were averaged to produce Fig. 2.38. The average of the $C_\mu$ distributions showed little variation in $C_\mu$ for both part span pipes. It is hypothesized that the one averaged data point which does not match the partial span $C_\mu$ data trend (PSP2 at 25 PSI) is the result of a change in jet velocity direction due to the higher pressure. Figure 2.38 also shows that increasing the exit area results in a decrease in $C_\mu$. This is due to lower exit jet velocities.

Table 2.5: Jet and freestream parameters required for $C_\mu$ and $F^+$ calculations.

| $U_\infty$ | $h$ [mm] | $C_{blade}$ [mm] | $x_{te}$ [mm] | $\rho_{jet}$ [kg/m$^3$] | $\rho_\infty$ [kg/m$^3$] |
|---|---|---|---|---|---|
| 36 | 1.52 | 76.20 | 64.77 | 1.225 | 1.255 |
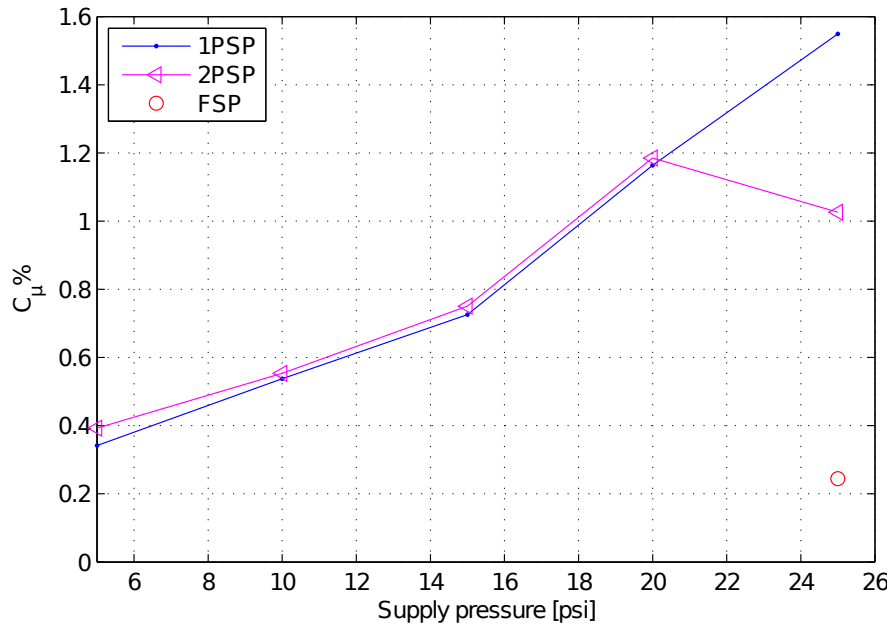


Figure 2.38: Average $C_\mu$ variation with supply pressure.

### 2.5.5 Baseline Flow Experiment

The baseline flow experiment was conducted to gather data on the NACA 0015 test blade for comparison with the flow control results, and to ensure that the measured pressure distributions match other experimental data. This experiment was completed using the cascade wind tunnel with a single, instrumented NACA 0015 test blade. Two test blade configurations were examined. The first used the FSP and no wing fences, and the second used the PSP1 and wing fences. The PSP1 pipe was used because it produced the highest values of $C_\mu$ in the jet characteristics experiment.

The pressure distributions were measured using a Barocell pressure transducer in conjunction with a scanivalve. The distributions were measured at multiple positive angles-of-attack and the corresponding negative angles. Due to symmetry, the pressure distributions taken at the negative angles were assumed to be equal to the pressure distributions on the bottom surface of the blade while at positive angles.

The lift coefficient $C_{L_{red}}$ versus angle-of-attack ($\alpha$) for both the FSP and the PSP1 test blades is shown in Fig. 2.39. The PSP1 $C_{L_{red}}$ curve indicates an abrupt stall at twelve degrees angle-of-attack. The FSP $C_{L_{red}}$ curve does not indicate a clear stall region.

The pressure distributions for angles-of-attack between twelve and seventeen are shown in Fig. 2.40. Stall is indicated by the flattening of the suction side pressure distribution near the trailing edge. Stall cell growth is apparent as the flatten region of the pressure distribution moves towards the leading edge when the incidence angle is increased.
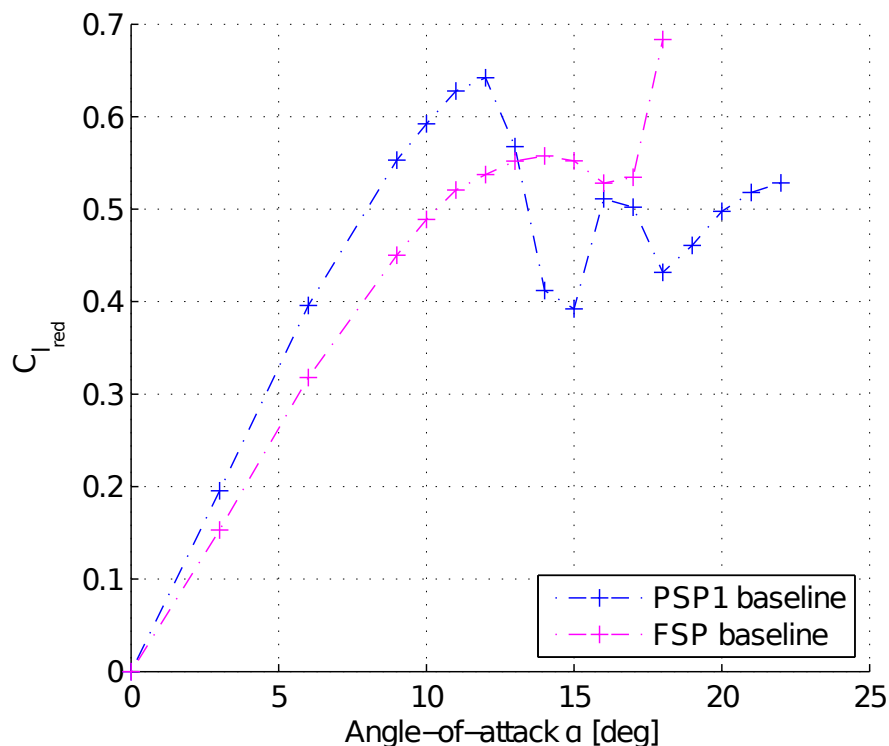
Figure 2.39: Lift coefficient vs. angle of attack for full- and part-span jet actuation.

Figure 2.40 shows that the PSP1 test blade begins to stall at twelve degrees angle-of-attack and that the stall cell moves towards the leading edge as the incidence angle is increased. This observed phenomena is consistent with other experimental studies (Seifert and Pack, 1999). Flattening of the suction side pressure distribution curve for the FSP test blade is minimal starting at fifteen degrees angle-of-attack. The PSP1 test blade displayed stall characteristics that matched trends found in some of our previous experiments (Traub et al., 2004). Because of its clear stall characteristics and large $C_\mu$ values, the PSP1 test blade was used for flow control experiments presented in the next section.

(a) $\alpha = 12°$

(b) $\alpha = 13°$

(c) $\alpha = 14°$

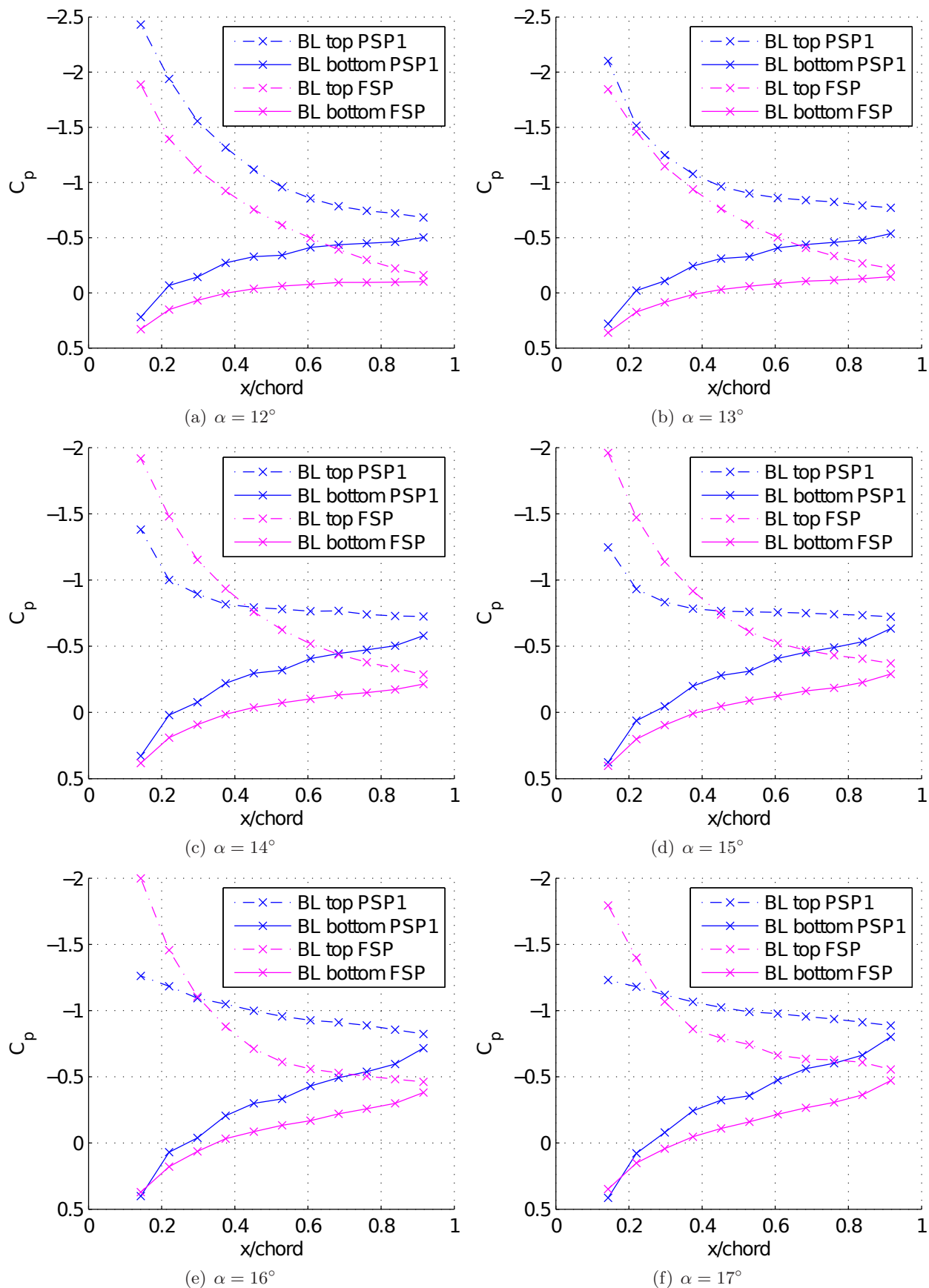(d) $\alpha = 15°$

(e) $\alpha = 16°$

(f) $\alpha = 17°$

Figure 2.40: Baseline pressured distributions.

### 2.5.6  Flow Control Experiment

The flow control experiment was conducted to test the effectiveness of the flow control system with different values of $C_\mu$ at an $F^+$ number of 0.47. Similar to the baseline flow experiment, the test was conducted in the cascade wind tunnel with a single instrumented test blade. However, unlike the baseline flow experiment, only the partial span test blade with wing fences (PSP1) was used.

The air used by the flow control system was provided by a high pressure supply tank. The supply pressure was controlled manually through the use of a valve system and pressure gauges. The supply pressure was allowed to stabilize before the test was conducted.

As with the baseline flow experiment, pressure distributions were measured using a Barocell pressure transducer in conjunction with a scanivalve. The pressure distributions were measured at several positive angles-of-attack. The reduced lift coefficient for each case was calculated using the same method as it was for the baseline flow experiment. The baseline pressure distributions from the corresponding negative angles-of-attack was assumed to be similar to the lower surface pressure distributions, and used to calculate the reduced lift coefficient. The test matrix for the flow control experiments can be seen in Table 2.6.

Table 2.6: Flow control test matrix.

| Blade Configuration | PSP1 |
|---|---|
| Angle-of-Attack [deg] | 0, 3, 6, 9, 10, 11, ... , 22 |
| Supply Pressure [psi] | 5, 10, 15, 20, 25 |

The calculated $C_{L_{red}}$ versus angle-of-attack was plotted for the baseline and flow control cases, and is shown in Fig. 2.41. The five flow control cases are shown in black while the baseline curve is colored blue for clarity. It is apparent from this plot that the stall angle-of-attack and the maximum $C_{L_{red}}$ are increased by the addition the pulsed width modulated flow control. A $\Delta C_{L_{red}}$ was calculated by subtracting the baseline $C_{L_{red}}$ from the flow control enhanced $C_{L_{red}}$ to better illustrate the improvement. A plot of $\Delta C_{L_{red}}$ for all five flow control cases can be seen in Fig. 2.42. It is apparent from Fig. 2.42 that the pulsed width modulated blowing has little effect on the lift characteristics prior to reaching stall. It was found that a substantial increase in $C_{L_{red},max}$ was achieved with even the smallest value of $C_\mu$, with an percent increase of 51.6%. A summary of the results for each of the five flow control cases can be seen in Table 2.7.

Table 2.7: Summary of results from flow control experiment.

| Supply Pressure [psi] | 5 | 10 | 15 | 20 | 25 |
|---|---|---|---|---|---|
| $C_\mu[\%]$ | 0.34 | 0.54 | 0.73 | 1.16 | 1.55 |
| % Increase $C_{L_{red},max}$ | 51.6 | 62.1 | 71.1 | 84.5 | 98.4 |
| $\Delta C_{L_{red}}$ | 0.332 | 0.400 | 0.456 | 0.543 | 0.632 |
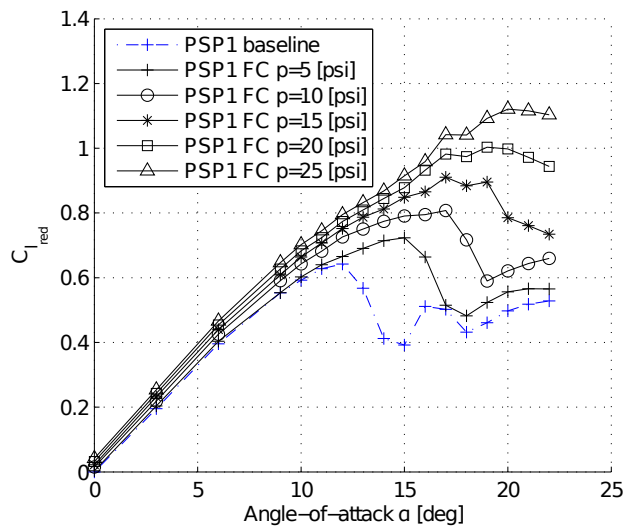
Figure 2.41: $C_{L_{red}}$ curves with flow control.
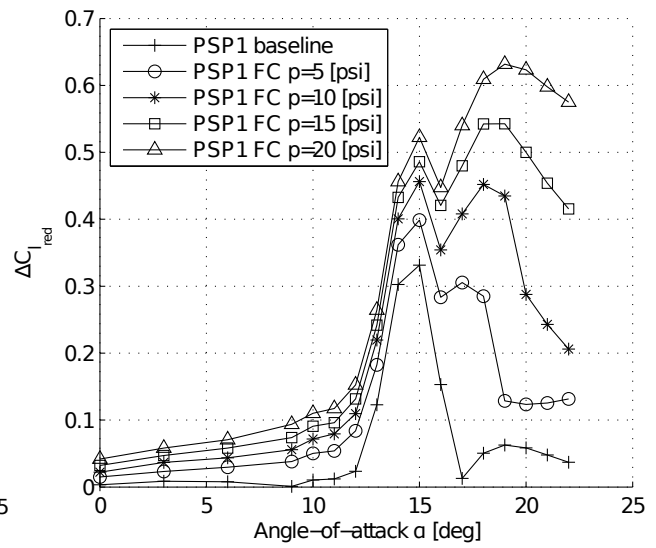


Figure 2.42: $\Delta C_{L_{red}}$ curves.

# Chapter 3

# Conclusions

The experimental investigation of oscillatory blowing actuation on cascade blades, supported by numerical simulation, demonstrated the capability of stall supression in a linear cascade. A crucial element of this flow control system was the pulse generator. This pulse generator uses the compressor rotation movement to generate high frequency oscillatory blowing actuation on the suction side of the airfoil. A scaled-down version of the pulse modulator was built and tested to ensure that the design would achieve the required flow parameters.

Several experiments were conducted with the scaled-down pulse modulator. Two sets of experiments studied the frequency response and the flow characteristics of the jet slot. Subsequently, a small wind tunnel with a linear cascade has been built around the scaled-down pulse modulator. These experiments studied the effects that oscillatory blowing had on the pressure distribution on the upper surface of a NACA 0015 airfoil section.

The frequency response experiment proved that, within the operating range of this compressor test rig and for reduced frequencies close to unity, jet frequency did not have a significant effect on $C_\mu$. The experimental investigation showed that jet slot exit area must match the area of the inlet to the internal plenum of the blade to obtain the $C_\mu$ values that are required to effectively suppress stall. It was also shown that the distribution of the holes in the internal pipe played an important role in the spanwise $C_\mu$ distribution, but it did not affect the mean $C_\mu$ value.

A subsequent experiment investigated the effect of oscillatory blowing actuation on a NACA 0015 in a wind tunnel that was build for a linear cascade of airfoils. In this experiment the pressure distribution on the suction side of the airfoil was measured with and without flow actuation. The investigation without oscillatory blowing actuation showed that (1) inner walls are needed to eliminate the non-uniform flow in the cascade and (2) the airfoil stalled between 12 and 13 degrees. When oscillatory blowing actuation was used, the lift coefficient increased by 51% to 98% and the angle-of-attack at stall increased by at least 5 deg.

Therefore, the experimental investigation conducted on the scaled-down pulse modulator demonstrated that it is worth building and testing the full-size pulse modulator for the compressor. Additional work is needed to understand the flow physics of the high frequency interaction between the oscillatory blowing actuation and the stall cell in order to suppress rotating stall. It appears that this research topic of using flow control is currently tackled by researchers in Europe (Nerger et al., 2010; Liesner et al., 2010). For the moment, they are using continuous blowing as opposed to oscillatory blowing, which gives us some advantage since continuous blowing is less effective that oscillatory blowing.

## Acknowledgment/Disclaimer

## Personnel Supported During Duration of Grant

| | |
|---|---|
| Paul G. A. Cizmas | Professor, Texas A&M University |
| Othon K. Rediniotis | Professor, Texas A&M University |
| Forrest Carpenter | Graduate Student, Texas A&M University |
| Shalom Johnson | Graduate Student, Texas A&M University |

## Publications

Journal articles:

- Kirk, A. M., Gargoloff, J. I., Rediniotis, O. K. and Cizmas, P. G. A., "Numerical and Experimental Investigation of a Serpentine Inlet Duct," *International Journal of Computational Fluid Dynamics*, Vol. 23, Issue 3, March 2009, pp. 245-258.

- Johnson, S., F. L. Carpenter., P. G. A. Cizmas, and O. K. Rediniotis, "Stall Suppression Using Oscillatory Blowing Actuation on Airfoils in a Cascade," *AIAA Journal of Propulsion and Power*, in preparation.

Conference papers:

- Johnson, S., F. L. Carpenter., P. G. A. Cizmas, and O. K. Rediniotis (2008, July). "Single-Stage Axial Compressor for the Study of Rotating Stall Suppression," *44th AIAA Joint Propulsion Conference & Exhibit*, Number 2008-4994, AIAA.

- Carpenter, F. L., S. Johnson, P. G. A. Cizmas, and O. K. Rediniotis (2009, January), "Internal plenum design and testing for an oscillatory blowing stall suppression system," In *47th AIAA Aerospace Sciences Meeting*, Number 2009-1242, AIAA.

## Honors and Awards Received

NONE

## AFRL Point of Contact

Dr. Steven Puterbaugh and Dr. Todd Bailie

# Bibliography

ABAQUS Inc. (2006). *ABAQUS 6.6-1.* ABAQUS Inc.

Carpenter, F. L., S. Johnson, P. G. A. Cizmas, and O. K. Rediniotis (2009, January). Internal plenum design and testing for an oscillatory blowing stall suppression system. In *47th AIAA Aerospace Sciences Meeting*, Number 2009-1242. AIAA.

Carter, C. J., S. A. Guillot, W. F. Ng, and W. W. Copenhaver (2001, July). Aerodynamic performace of a high-turning compressor stator with flow control. In *37th AIAA/ASME/SAE/ASEE Joint Propulsion Conference and Exhibit*, AIAA-2001-3973, pp. 1–6. American Institute of Aeronautics and Astronautics.

Chima, R. V. (2003a). Swift - multiblock analysis code for turbomachinery, ver. 300. NASA Glenn Research Center, Cleveland OH.

Chima, R. V. (2003b). Tcgrid 3-d grid generator for turbomachiery ver. 300. NASA Glenn Research Center, Cleveland OH.

Culley, D. E., M. M. Bright, P. S. Prahst, and A. J. Strazisar (2004, January). Active flow separation control of a stator vane using embedded injection in a multistage compressor experiment. *Transaction of the ASME - Journal of Turbomachinery 126*(1), 24–34.

Day, I. J. (1993a, January). Active suppression of rotating stall and surge in axial compressors. *ASME Journal of Turbomachinery 115*(1), 40–47.

Day, I. J. (1993b, September). Review of stall, surge and active control in axial compressors. In *Eleventh International Symposium on Air Breathing Engines*, Tokyo, Japan, pp. 97–105. AIAA.

Epstein, A. H., J. E. Ffowcs-Williams, and E. M. Greitzer (1989, March-April). Active suppression of compressor instabilities. *Journal of Propulsion and Power 5*(2), 204–211.

Florea, R., K. C. Hall, and P. G. A. Cizmas (1997). Eigenmode analysis of unsteady viscous flows in turbomachinery cascades. In T. H. Fransson (Ed.), *Proceedings of the 8th International Symposium on Unsteady Aerodynamics and Aeroelasticity of Turbomachines*, Stockholm, Sweden, pp. 767–782.

Florea, R., K. C. Hall, and P. G. A. Cizmas (1998). Reduced-order modeling of unsteady viscous flow in a compressor cascade. *AIAA Journal 36*(6), 1039–1048.

Gargoloff, J. I., P. G. A. Cizmas, T. W. Strganac, and P. S. Beran (2006, May). Parallel algorithm for fully nonlinear aeroelastic analysis. In *47th AIAA/ASME/ASCE/AHS/ASC Structures, Structural Dynamics, and Materials Conference*, AIAA Paper 2006-2073, Newport, Rhode Island.

Greitzer, E. M. (1978, April). Surge and rotating stall in axial flow compressors. *ASME Journal of Engineering for Power 98*, 190–217.

Han, Z. and P. G. A. Cizmas (2003, January). Prediction of axial thrust load in centrifugal compressors. *International Journal of Turbo & Jet-Engines 20*(1), 1–16.

Johnson, S., F. L. Carpenter, P. G. A. Cizmas, and O. K. Rediniotis (2008, July). Single-stage axial compressor for the study of rotating stall suppression. In *44th Joint Propulsion Conference and Exhibit*, Number 2008-4994. AIAA.

Liesner, K., R. Meyer, M. Lemke, F. Thiele, and C. Gmelin (2010, June). On the efficiency of secondary flow suction in a compressor cascade. In *TurboExpo 2010, International Gas Turbine Institute Conference*, Number GT2010-22336, Glasgow, Scotland, UK.

Menter, F. R. (1994). Two-equation eddy-viscosity turbulence models for engineering applications. *AIAA Journal 32*(8), 1598–1605.

Moore, F. K. and E. M. Greitzer (1986, January). A theory of post-stall transients in axial compression systems: Part i - development of equations. *Transactions of the ASME - Journal of Engineering for Gas Turbines and Power 108*(1), 68–76.

Nerger, D., H. Saathoff, R. Radespiel, V. Gummer, and C. Clement (2010). Experimental investigation of endwall and suction side blowing in a highly loaded stator cascade. In *TurboExpo 2010, International Gas Turbine Institute Conference*, Number GT2010-22578, address = Glasgow, Scotland, UK, month = June.

Paduano, J. D., A. H. Epstein, L. Valavani, J. P. Longley, E. M. Greitzer, and G. R. Guenette (1993). Active control of rotating stall in a low-speed axial compressor. *Transactions of the ASME - Journal of Turbomachinery 115*, 48–56.

Seifert, A. and L. Pack (1999, January). Oscillatory excitation of unsteady compressible flows over airfoils at flight reynolds number. In *37th Aerospace Science Meeting and Exhibit*, AIAA Paper 99-0925.

Silkowski, P. D. (1990). Aerodynamic design of moveable inlet guide vanes for active control of rotating stall. Master's thesis, Massachussetts Institute of Technology.

Suder, K. L., M. D. Hathaway, S. A. Thorp, A. J. Strazisar, and M. B. Bright (2001, January). Compressor stability enhancement using discrete tip injection. *Journal of Turbomachinery. Transactions of the ASME 123*(1), 14–23.

Traub, L., A. Miller, and O. K. Rediniotis (2004, September-October). Effects of synthetic jet actuation on a pitching NACA 0015 wing. *Journal of Aircraft 41*(5), 1153–1162.

White, F. M. (2006). *Viscous Fluid Flow* (3 ed.). McGraw Hill.